Electroactive Properties and Biological Applications of Electrospun PVDF Polymer

Dissertation submitted to the University of Madeira in fulfillment of the requirements
for the degree of Master in Nanochemistry and Nanomaterials
by Xiang Yao

Work developed under the supervision of
Professor Dr. Pedro Filipe Duarte Louzeiro Pires and
co-supervised by Professor Dr. Helena Maria Pires Gaspar Tomás

Faculdade de Ciências Exatas e de Engenharia,
Centro de Química da Madeira,
Campus Universitário da Penteada,

Funchal – Portugal
November 2016

DECLARATION

I hereby declare that this thesis is the result of my own work, is original and was written by me. I also declare that its reproduction and publication by Madeira University will not break any third party rights and that I have not previously (in its entirety or in part) submitted it elsewhere for obtaining any qualification or degree. Furthermore, I certify that all the sources of information used in the thesis were properly cited.

Funchal, 14th of October 2016

XIANG YAO

ACKNOWLEDGEMENTS

I would like to express my gratitude to all those who helped me during the writing of this thesis.

My deepest gratitude goes first and foremost to Professor Pedro Pires, my supervisor, for his constant encouragement and guidance. He has walked me through all the stages of my research and writing of this thesis. Without his consistent and illuminating instruction, this thesis could not have reached its present form.

I would like to express gratitude to Professor Helena Tomás, who led me into the world of cells. She gave me all the support to needed in the cell tests.

I also owe special gratitude to Ana Olival, who gave me strong support during cells cytotoxicity that I have done. Thank you for your patience with me who did not know anything in the beginning. Moreover, I learn from you what responsibility is.

Thanks to the SEM characterizations supported by textile college in Donghua University in Shanghai China. I also appreciate the help from Wuhan Textile University in Wuhan China for supporting the rotational rheometer (Kinexus, Malvern Instruments Ltd) and electrospinning apparatus (SS-3556H, Beijing Ucalery tech Co.Ltd).

I would like to thank all members of the Molecular Materials Research Group (MMRG) of Centro de Química da Madeira (CQM) for all the support and friendship.

This master project was supported by *Fundação para a Ciência e a Tecnologia* (FCT) through the CQM Strategic Project PEst-OE/QUI/UI0674/2014.

CONFERENCE CONTRIBUTIONS

April 2016 – Oral Presentation:

Xiang Yao, Ana Olival, Pedro Pires, Helena Tomás, Electroactive Properties and Biological Applications of Electrospun PVDF Polymer, presented at the 3rd CQM Annual Meeting/11th Materials Group Meeting – 01th-02nd of April 2016 - University of Madeira, Funchal, Portugal.

ABSTRACT

PVDF is a piezoelectric polymer, exhibiting direct and inverse piezoelectric effect, with leading electroactive properties. This material is interesting for building energy transmission and harvesting systems, converting mechanical energy into electrical energy, such as electrospun PVDF sensors. However, only a few reports have shown inverse piezoelectric effect of electrospun PVDF.

In this project the electrospinning technique was used to prepare PVDF nanofiber mat scaffolds for tissue engineering. The main objective is the preparation of electroactuated devices for mechanical stimulation of cells.

Crystal phase ratios and morphology of the PVDF fiber mats were characterized by attenuated total reflectance Fourier transform infrared (FTIR/ATR) spectroscopy and scanning electron micrograph (SEM). For a better understanding of the differences between polar and non-polar PVDF, and of the effect of the electric field on the fibers' composition, quantum mechanics and molecular dynamics calculations were performed. Several devices were prepared from assemblies of PVDF fiber meshes and conductive ink electrodes, with different geometries. The devices' electrical impedances were measured as a function of frequency. Finally, the in vitro biocompatibility of the PVDF fiber meshes was tested.

The results revealed that electrospinning parameters have significant effects on the crystal phase ratio and structure. As it was expected, the electrical impedance of PVDF decreased with the increase of β crystal phase ratio, as required for the piezoelectric behaviour of the PVDF fibers. The results also illustrated that the impedance of PVDF fibers mesh assemblies changed with varying shape, thickness, the geometric alignment of the fibers and the distance between conductive ink electrodes.

The molecular simulations were able to predict the α to β phase change which results on partially poled fibers. In vitro cytocompatibility tests of PVDF scaffolds shown that PVDF fibers were not cytotoxic to the NIH/3T3 cells which meant PVDF fiber scaffolds can be used for cell stimulation.

Keywords: PVDF (polyvinylidene fluoride); electrospinning; electroactuator; impedance; cytocompatibility .

RESUMO

O PVDF é um polímero piezoelétrico, que exibe o efeito piezoelétrico direto e indireto. Este material é interessante para construção de sistemas para conversão ou captação de energia mecânica para energia elétrica, tais como sensores baseados em fibras preparadas por electrospinning. No entanto, têm sido reportados poucos trabalhos sobre o efeito piezoelétrico inverso de fibras de PVDF.

Neste projeto, utilizou-se a técnica de electrospinning para preparar estruturas constituídas por tapetes de nanofibras de PVDF, para engenharia de tecidos. O objetivo principal é a preparação de dispositivos eletroatuados para estimulação mecânica de células.

A morfologia e a razão entre estruturas cristalinas dos tapetes de fibras de PVDF foram caracterizados por espectroscopia de infravermelho por transformada de Fourier – reflectância total atenuada (FTIR/ATR) e microscopia eletrónica de varrimento (SEM). Para uma melhor compreensão das diferenças entre o PVDF polarizado e não-polarizado, assim como o efeito do campo elétrico na composição das fibras, realizaram-se cálculos de mecânica quântica e dinâmica molecular. Foram preparadas várias montagens de tapetes de fibras de PVDF em elétrodos de tinta condutora, com diversas geometrias. As impedâncias elétricas dos dispositivos foram medidas em função da frequência. Finalmente, foram realizados testes in vitro para atestar a biocompatibilidade das fibras de PVDF.

Os resultados demonstram que os parâmetros operacionais do electrospinning têm efeitos significativos na estrutura das fibras e na estrutura cristalina. Como se esperava, a impedância elétrica do PVDF decresce com o aumento da fase cristalina α, condição necessária para o comportamento piezoelétrico das fibras. Os resultados também ilustram a dependência que a impedância, dos dispositivos com fibras de PVDF, apresenta em função da forma, espessura, alinhamento das fibras e distância entre elétrodos.

As simulações moleculares conseguiram prever a mudança de fase α para β, que resultam em fibras com polarização parcial. Os testes de citocompatibilidade in vitro, demonstraram que os tapetes de fibras de PVDF não apresentam efeitos citotóxicos para as células NIH/3T3, o que significa que os dispositivos de fibras de PVDF podem ser utlizados para estimulação de células.

palavra chave: PVDF; electrospinning; eletroatuados; impedância; citocompatibilid.

CONTENTS

LIST OF FIGURES

LIST OF TABLES

LIST OF FORMULAS

LIST OF ABBREVIATIONS

°C	Celsius
AC	Alternating Current
ATR	Attenuated Total Reflection
BTEAC	Benzyl Triethyl Ammonium Chloride
C	Capacitance
CPE	Conductive Plastic Electrode
DC	Direct Current
DMF	Dimethyl Formamide
ECM	Extracellular Matrix
EDTA	Ethylene Diamine Tetraacetic Acid
EIS	Electrochemical Impedance Spectroscopy
F	Frequency
FTIR	Fourier Transform Infrared
kV	kilo Voltage
L	Length
MHz	Megahertz
MTS	a colorimetric assay for assessing cell metabolic activity
MTT	a colorimetric assay for assessing cell metabolic activity
PAMAM	Polyamidoamine Dendrimer
PBS	Phosphate Buffered Saline
PLGA	Polylactic-co-Glycolic Acid
PMMA	Polymethyl Methacrylate
PVDF	Polyvinylidene fluoride

R	Resistance
A	Surface Area
S	Solvent
SEM	Scanning Electron Microscope
SP	Specific
T	Thickness
TrFE	Trifluoroethylene
UC	University of California
W	Width
XTT	a colorimetric assay for assessing cell metabolic activity
Z	Impedance
ρ	Resistivity

CHAPTER 1-INTRODUCTION

1.1 PVDF

1.1.1 Crystalline phase structure of PVDF

Polyvinylidene fluoride, abbreviated as PVDF, results from the polymerization of $CH_2 = CF_2$ monomers, where two hydrogen atoms of ethylene were substituted by fluorine atoms. PVDF polymer chains exist in five different possible crystalline phases, which are represented by α, β, γ, δ, ε. Among them, α and ε are non-polar and the other three are polar. The differences arise from several possible values of the torsional angle between consecutive monomer unit cells, which results on different chain conformations [1-5]. Since fluorine atoms are more electronegative than carbon and hydrogen, they can be assigned negative point charges. Being the less electronegative, hydrogen atoms are positively charged, whereas carbon atoms are divided into positive or negative, if they are bonded to fluorine or hydrogen, respectively. This simple reasoning can be confirmed by semi empirical quantum mechanics simulations of small polymer chains, as represented in Fig 1. As a consequence, the dipole moments associated to the CH_2 or CF_2 groups of consecutive polymer unit cells, can totally cancel each other (α phase), sum up (β phase), or anything in between, resulting in different phase behavior.

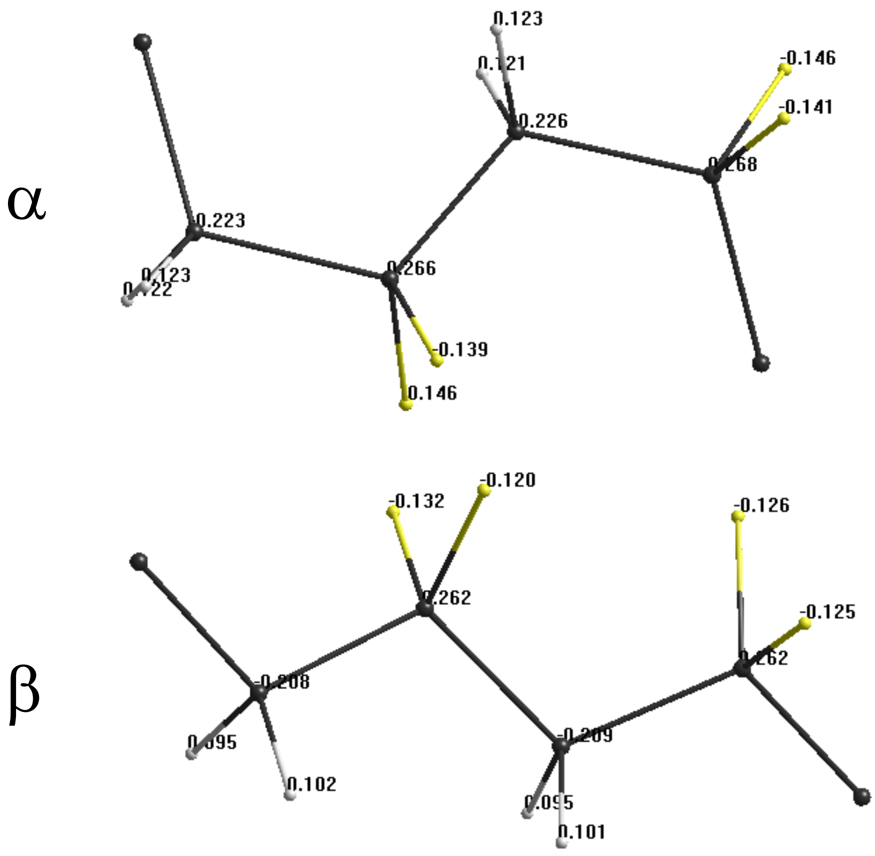

Fig. 1: Atomic point charges predicted by PM3 semi empirical quantum mechanics calculations for PVDF polymer chains with 8 unit cells (white, black and yellow represent hydrogen, carbon and fluorine, respectively).

As shown in Fig. 2, the dipole moment in the non-polar α phase is randomly oriented, whereas in the polar β phase all dipole moments have the same orientation. In long polymer chains, different conformations can be found, between full non-polar α, full polar β and a mixture of α and β domains. The percentage of polar domains, or the ratio between polar and non-polar domains, can be expected to affect the overall electric properties and the electrostrictive behavior of a given PVDF macroscopic sample.

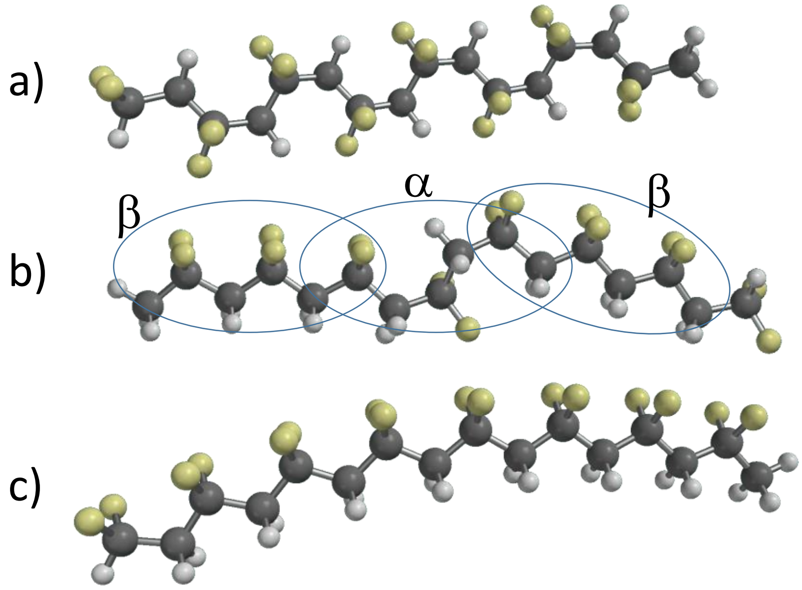

Fig. 2: a) Full α polymer chain; b) Polymer chain with mixed α and β domains; c) Full β polymer chain (white, black and yellow represent hydrogen, carbon and fluorine, respectively).

However, the different crystalline phases can be converted to each other by application of different conditions, such as temperature or pressure annealing, electric field poling, or mechanical stress, as we can see from Fig. 3 [2,3,4]. If no such special conditions are used, PVDF produced under normal conditions is, usually, non-polar, because the molecular polymer chains are randomly oriented in alternate directions. For example, film casting is one of the methods to produce PVDF film, and in this case, the α phase is the main conformation. To prepare polar PVDF a significant percentage of the dipole moments must be forced to face the same direction, or the polymer chains must be stretched in some way.

Electric-field poling is the most used method for production polar PVDF films and meshes. The PVDF sample is placed between two electrodes and heated to a temperature below the glass transition to increase mobility and allow the rearrangement of torsional angles in the polymer chains. A strong electrostatic field in the kilovolt range, applied between the electrodes, forces the reorientation of intramolecular dipoles resulting on the overall polarization of the polymer chains. When the temperature is lowered the polymer becomes frozen in the polarized state. Experimental results and our own theoretical calculations suggest the α non-polar state has a slightly lower energy than the polar β state. Since the random organization of dipoles in the α state make it higher entropic than the ordered β state, the former is expected to be thermodynamically more stable. This idea will be further elaborated in this work's conclusions. Anyway, any factors which may impact on the final PVDF structure (film, mesh, or other), such as polymer composition and chain size, solvents or doping agents, are expected to modify its properties[5].

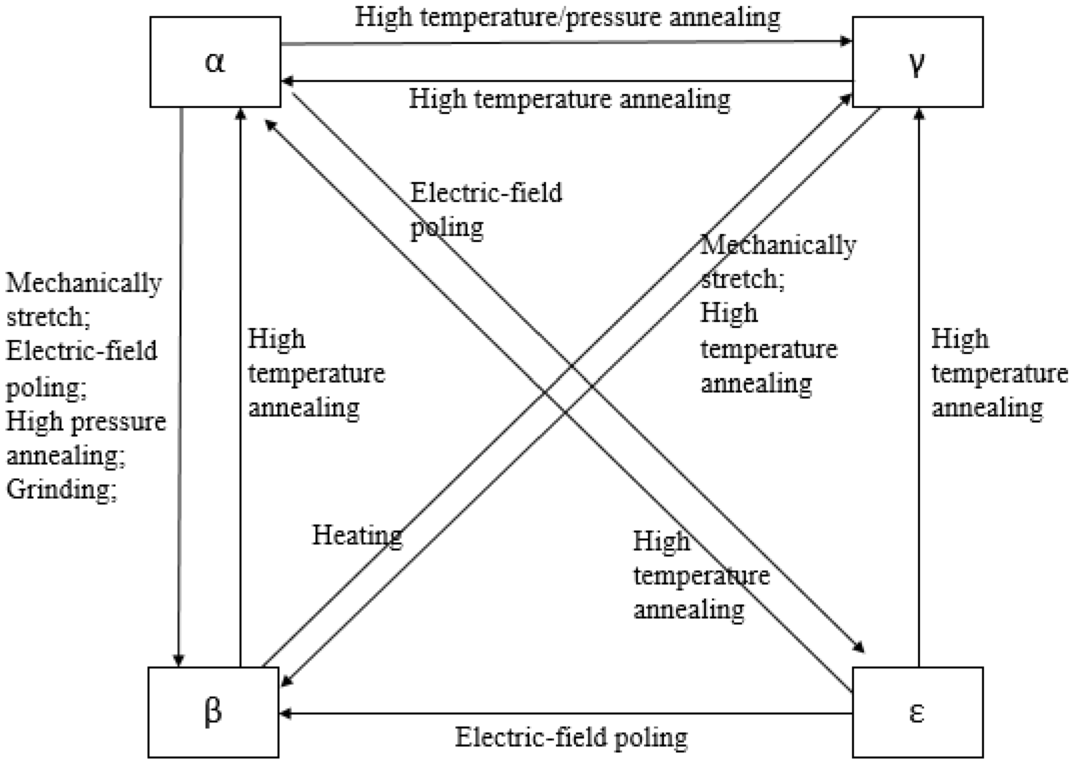

Fig. 3: The conversion between four different crystal phases. [2,3,4]

1.1.2 Piezoelectric effects of PVDF

As with all dielectric (non-electrical conductor) materials PVDF also exhibits electrostrictive behavior, suffering a mechanical deformation when an electrical field is applied. Electrostriction is quite similar to the piezoelectric effect but there are two main differences. First, the mechanical deformation of electrostrictive materials has a quadratic dependence from the electric field, whereas piezoelectricity is linear. As consequence of the quadratic dependence, the inversion of the electric field produces the same effect. Secondly, the mechanical deformation of piezoelectric materials produces an electric field perturbation, but the same is not valid for electrostriction. Although the two effects are different, and piezoelectricity is not typical from polymers, poled PVDF with dominant β crystalline phase does behave as a strong piezoelectric material[3].

The mechanism of PVDF's direct and inverse piezoelectric effect is shown in Fig. 4, Direct piezoelectric effect produces electric polarization as a result of applied mechanical deformation, such as stress or compression. The polarization can be interpreted as resulting from repulsion between atomic point charges of adjacent polymer chains and not from effective electric charge displacement. The inverse piezoelectric effect generates mechanical deformation as result of the polymer chains realignment under an applied electric field. For both direct and indirect effects, the polarization degree of the β crystalline phase plays an important role in determining the intensity of the piezoelectric effect[6].

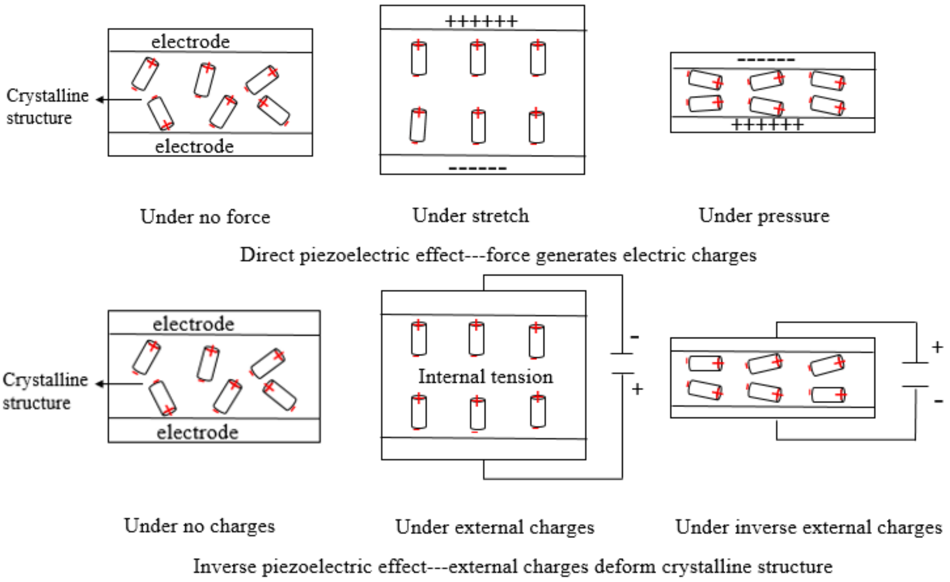

Fig. 4: Schematic of direct and inverse piezoelectric effect[2].

1.2 Electrospinning process

Electrospinning has been developing for decades and has attracted more and more interest from researchers in various fields, for being a convenient method for nanofiber manufacturing, of different materials, with different structures and properties[6-10]. The nanoscale, fine and with high specific surface area, give electrospun nanofibers a great potential for application in biology, engineering, tissue engineering, catalysis, energy storage, electrical engineering, smart devices and so on.

Generally, as shown in Fig. 5 (a), a simple electrospinning setup just requires four necessary parts, including direct current high voltage, mental hollow needle, a syringe pump, and a grounded or negative charged collector. Wherein the mental needle has to be connected with voltage supply, giving a high electrical potential between needle and collector, resulting in charged liquid at the top of needle. The syringe pump is used to control liquid flow speed especially for low viscosity solutions. When this electrostatic force is high enough to overcome the liquids' surface tension, the flow jet is stretched out of the needle. There is a critical point in the surface of droplet called Taylor cone. Reznik[11] et al. described the shape of the Taylor cone precisely at the first time. They believed that the shape of cone was contributed to the ratio of electrostatic repulsion to surface tension. Then the jet was elongated due to electrostatic repulsion in bended fibers, meanwhile it dries in flight because of solvents' evaporation until deposited on collector. As the uniformity and thickness distribution result from the fibers bending instability, the morphology of fibers could be adjusted by different parameters, such as polymer components, viscosity, voltage values, collecting distance and so on.

For standard electrospinning apparatus used in laboratory, applied voltage is normally less than 30 kV, unless the syringe pump could not feed enough stocks. It is also highly dependent on humidity; this is why the advanced electrospinning setups are usually covered by a chamber. The temperature accelerates evaporation of solvents as well, which is considered into electrospinning setup design. The fiber productivity is close to 300 mg per hour[12]. Depending on recently developed electrospinning techniques, the diameters of electrospun fibers are in range of 10 nm to 1 µm.

In this project, two electrospinning setups were used for preparing PVDF nanofibers. Fig. 5 (b) was belong to Wuhan Textile University, Fig. 5 (c) was belong to Madeira University. In principle, these two setups were the same. All the samples were characterized by same methods under the same conditions.

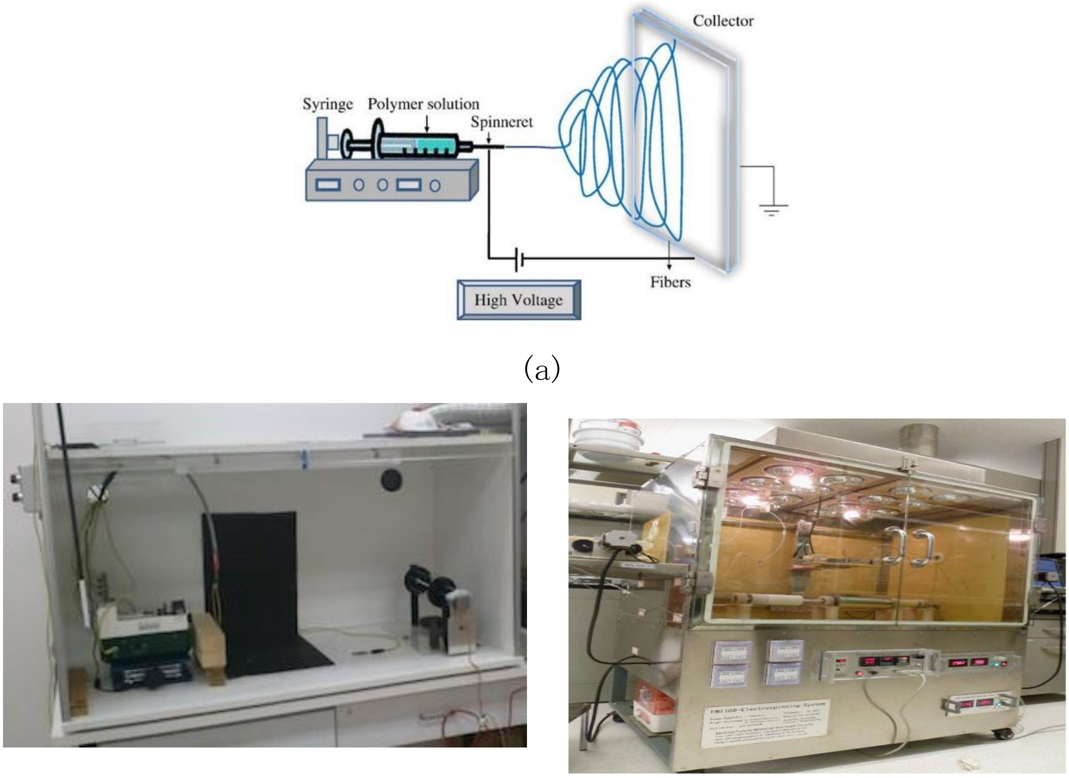

(a)

(b) (c)

Fig. 5: (a) Schematic representation of an electrospinning apparatus[10]; (b) and (c) Real apparatus.

1.3 The progresses in Electrospinning PVDF nanofibers

1.3.1 Normal electrospinning for PVDF nanofibers

There were a lot of researchers have done some work in electrospinning PVDF nanofibers. Renuga Gopal et al[7] prepared PVDF nanofiber membranes by electrospinning process, and use heat treatment process to maintain the structure of the fiber membranes. The diameter of obtained fibers was around 380 nm. The filtration efficiency of this fiber membrane to 1 μm polystyrene particles was up to 98%. Zhe-Qin Dong et al[8] prepared PVDF - PTFE composite nanofiber membranes by electrospinning, to desalinate seawater. The fibers' diameter was about 500 nm. Cao Jianhua et al[9] made PVDF and PVDF-hexafluoropropylene copolymer blended nanofiber electrolyte membrane, with a diameter distribution between 300-700 nm. Yuan Xiaoyan et al[13] dissolved PVDF polymer in DMF and acetone mixed solvent, and electrospun PVDF ultrafine nanofibers with 50-500 nm diameters. These fibers received a continuous heat treatment process to enhance their mechanical properties. They also prepared PVDF / polycarbonate composite ultrafine fibers with a core/sheat structure, by adding PMMA or BTEAC into the spinning solution, modifying the polymer electrolyte to form a uniform morphology and the core/sheat structure. The fibers obtained had a diameter of 300-500 nm.

1.3.2 Near-field electrospinning for PVDF fibers

Pan, C. et al[14], applied a near-field electrospinning technique to produce hollow-walled PVDF nanofibers for a nanoscale energy generator. Fig. 6 shown the process for preparing the device by near field electrospinning. They dissolved PVDF polymer in a mixed solution of dimethyl sulfoxide and DMF with concentrations in range of 5-20 wt%. The viscosity of polymer solution was too low for electrospinning when the concentration was less than 10wt%, and when the concentration was higher than 20 wt%, the viscosity is too high for electrospinning. They report the concentration between 12.5-15 wt% to be the optimal for electrospinning. In some cases, they added acetone into the mixture to improve the solvent's volatility[15-16].

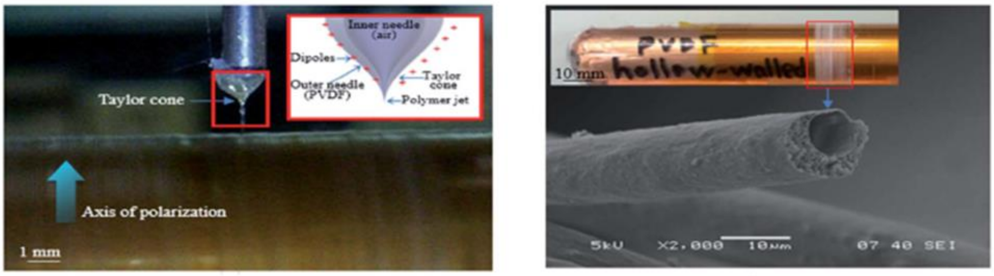

(a) (b)

Fig. 6: Near field electrospinning for nanogenerator[13].

The advantages of near field electrospinning are on the precise control of the nanoscale fibers orientation, keeping the device as small as possible, and, at the same time, avoiding the offset of polarity between nanofibers. Another benefit of this process was that the latest and advanced near-field electrospinning technique enabled the PVDF nanofibers to be directly deposited on the device's electrodes. This direct writing technology is convenient and precise for controlling different sizes and parameters, and also exhibits potential for mass production. Chieh et al[1] in UC Berkeley also prepared a PVDF energy generator by near-field electrospinning technique, as shown in Fig. 7. When they applied 0.092% external strain on a single PVDF electrospun fiber, repeated and continuous 8.5 mV output voltage was generated, the corresponding output power reached almost 7.2 pW. They believe this technique to have an unprecedented potential for direct conversion of mechanical strain into electric energy capture, as well as for pressure sensors manufacturing.

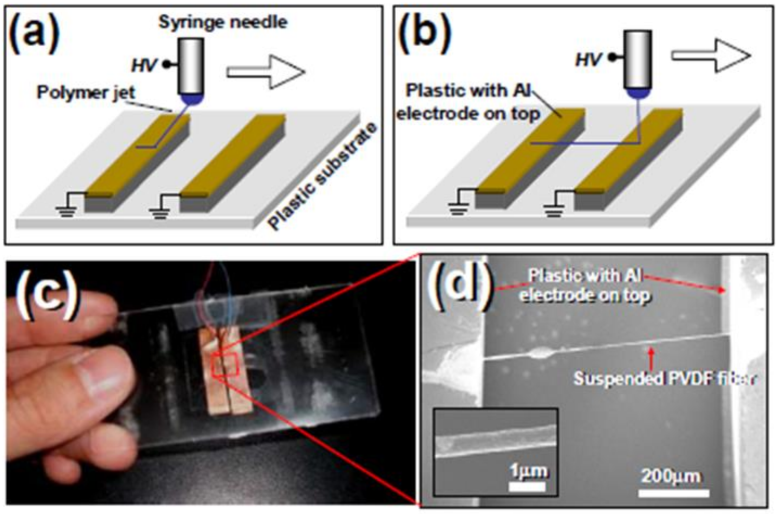

Fig. 7: (a), (b) Fabrication process of PVDF nanogenerator via NFES. (c) Photo of PVDF nanogenerator on a plastic substrate. (d) SEM picture showing a suspended PVDF nanofiber with diameter of 700nm[1].

To be more specific, two aluminium electrodes were placed on a plastic substrate, the space between the electrodes was in range from 500 µm to 1 mm, where the aluminium electrode is used to receive nanofibers directly. The aluminium electrodes were connected to the test equipment. Conductive silver was coated on the surface of the PVDF nanofibers, which reduced the contact resistance. They also researched the impact of different experimental parameters on the piezoelectric effect of the PVDF nanofibers, including flow speed of spinning jet, polymer solutions' concentration, collector rotating speed, and electric-field intensity.

1.3.3 Effect of experimental electrospinning parameters on PVFD nanofibers

For a successful electrospinning process, the polymer solution intrinsic properties are very important are relate strongly to the morphology of electrospun fibers. Although the list of solution intrinsic properties includes many factors, such as molecular weight, surface tension, concentrations and so on, not all these parameters are independent from each other and crucial for the process, therefore researchers usually focus on rheological properties[17].

Since the electrospinning process uses an intense electrostatic field between the needle and the collector, it is a straightforward idea to use this strong electric field to convert α crystalline phase PVDF into β crystalline phase[1,7,8]. The poling process starts from the jet flowing out of the needle and continues throughout the flight to the collector, with the intense electric field, stretching the dipole moments into same direction until the solvent evaporates, the polymer chain mobility decreases and the fibers land in the collector. The process depicted in Fig. 8, is named *in situ poling process*, because the poling and spinning occur simultaneously. The result is a fiber mesh composed of PVDF fibers with a mix of polar β and non-polar α domains, the ratio of the two (β/α ratio) depending upon the experimental parameters.

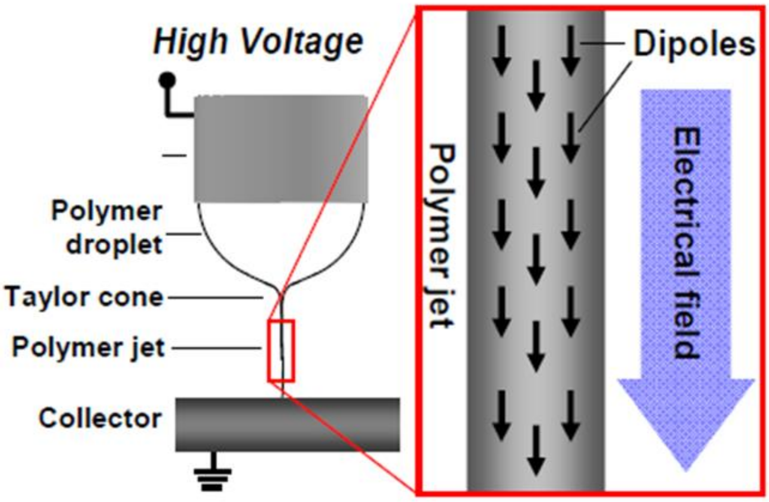

Fig. 8: Schematic of the electrospinning and in-situ poling process[1].

However, some reports indicate that the electrospinning parameters have significant effects on the β/α ratio. For example, Shao, H. et al[5] prepared PVDF electrospun nanofiber meshes. They studied the impact of parameters, such as, voltage, spinning distance, concentration of the spinning solution, the β/α ratio and nanofiber mat thickness, on the piezoelectric effect of the PVDF meshes. The results show that when the fibers are smaller and more uniform, its β/α ratio is higher and the piezoelectric output voltage of PVDF meshes is the higher, regardless of concentration and other parameters. The output voltage and current correlate directly with the β/α ratio, no matter which electrospinning parameter are used. This means the β/α ratio is the sole and independent factor affecting the energy conversion efficiency of the PVDF meshes. Abolhasani, M. et al[18] enhanced the PVDF piezoelectric output by adjusting electrospinning parameters. They studied the impact of different ratios between DMF and acetone on the poling efficiency. They also found that high rotating speed of the collector enhanced the β/α ratio, because the high speed rotation favored a specific orientation of the deposited fibers. Different solvents, or differences in the volume ratio with same solvents both resulted in a big difference for fiber morphology. For example, dimethyl sulfoxide and DMF can be used as the solvents of PVDF polymer, but addition of acetone is necessary to improve the solvents volatility; the spinnability of PVDF polymer solutions is higher when the mixture of dimethyl sulfoxide and DMF has a weight ratio of 8:2 with acetone[5.16]. However, adding too much acetone, the fiber morphology is inadequate, with beads forming in the fibers, because of excessively fast drying and not enough stretching. Using only DMF and acetone as solvent also results on better evaporation rate of the mixed solvents and better fiber morphology.

None of the studies on PVDF electrospinning gives a definite theoretical framework for the mechanism of α to β PVDF conversion, neither clarify if the conversion happens: in solution; at the Taylor cone surface; or in-flight (during the early liquid state stage or later solid state). Nevertheless, it is clear that the strong electrostatic field exerts force upon the different groups' dipole moments, eventually triggering the spontaneous change of torsional angles to a more favorable state. This change is energetically driven, since the high β/α ratio is entropically disfavored, and takes advantage of the high mobility of single polymer chains during the electrospinning process and subsequent *freezing* in the solid fiber mesh.

The infrared spectrum of PVDF samples has been studied. The α and β crystalline phases have slightly different spectra, with a few normal modes of vibration in clean areas of the spectrum, which allows for differential determination of the β content in PVDF solid samples by FTIR. It is the case of absorption bands at: 765 cm^{-1} (CH_2 in-plane bending), 878 cm^{-1} (CH_2 out-of-plane bending), 1073 cm^{-1} and 1182 cm^{-1} for α crystalline phase; 841 cm^{-1} (CF_2 asymmetrical stretching) and 1278 cm^{-1} (C–F stretching vibrations) for β phase[19].

According to Lambert - Beer law, the fraction of β phase can be calculated from the following formula[18].

$$F(\beta) = F(\beta)\frac{A_\beta}{1.26A_\alpha + A_\beta} \quad （1）$$

Where, A_α and A_β represent the absorption intensity at wavelength of 765 cm^{-1} and 841 cm^{-1}, respectively, as pictured in Fig. 9[18,19].

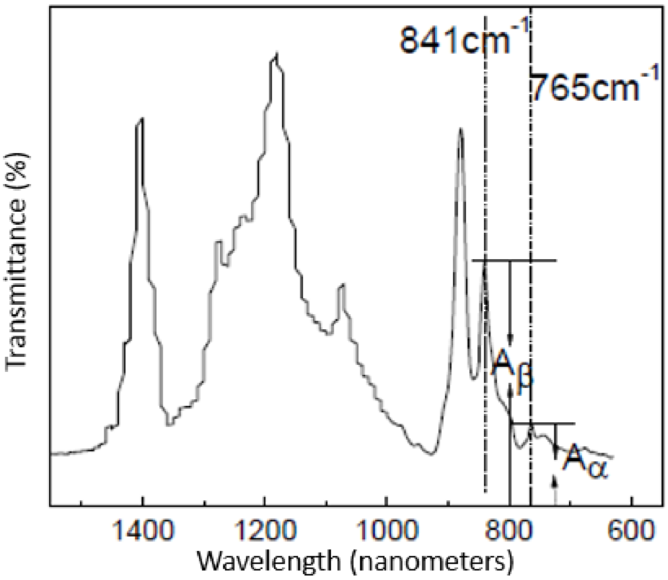

Fig. 9: Absorption intensity of PVDF FTIR spectrum in wavenumber of 765 cm^{-1} and 841 cm^{-1}.

Meanwhile, according to the conversion formula between the infrared absorbance and transmittance, we can convert experimental absorbance into transmittance and calculate the ratio of β phase with Lambert-Bill formula.

1.4 Applications of PVDF for inverse piezoelectric effect

There are not many researches about inverse piezoelectric effect of PVDF recently[20,21]. Chocat et al[20] used a pre-forming heat drawing technique to produce up to kilometer ultrafine fibers, of a PVDF and trifluoroethylene copolymer, embedded in polycarbonate, as shown in Fig. 10, for application on acoustic emission and detection. To be noted, the scope of the acoustic signal spectrum was quite wide, from tens of Hz to tens of megahertz.

As the PVDF fiber mesh is flexible, it can easily be assembled into large dimension structures such as, fabric, reticulate structures or mounted on surface electrodes. To achieve miniaturization and flexibility at the same time, electrodes with different geometric shapes can be designed, like in Fig. 11.

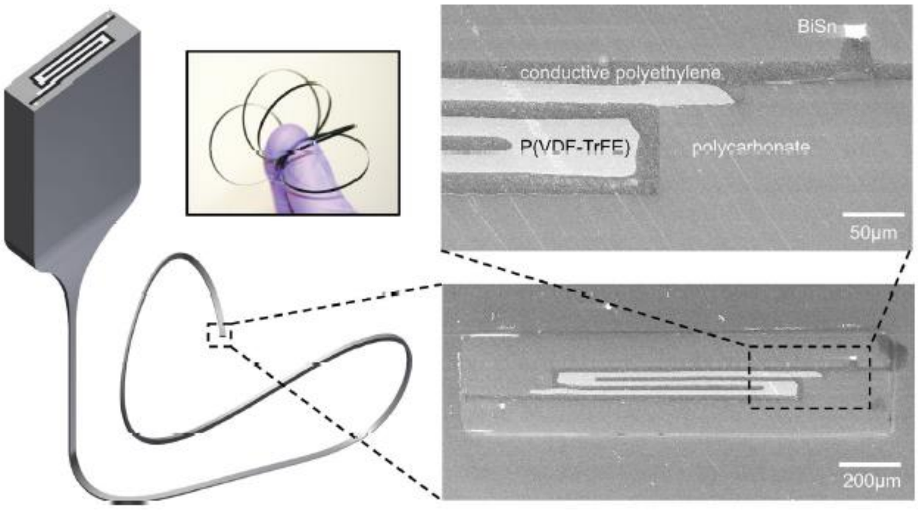

Fig. 10: Schematic drawing of a preform drawn into a fiber along with SEM microscopy images of a piezoelectric fiber and magnification. Inset: Flexible piezoelectric-stack fiber[20].

Fig. 11: Different geometric shapes and designs of conductive electrode.

Such a device can generate electric energy from acoustic energy by direct piezoelectric effect, also generate acoustic energy from electric energy by inverse piezoelectric effect. It was very sensitive because of the untrafine and folded structure.

1.5 Electrical properties of PVDF

1.5.1 Impedance principle and modeling

Alternant current impedance was also called EIS (Electrochemical Impedance Spectroscopy, abbreviated as EIS). Impedance measurement was a method originally used to study frequency response in linear circuit networks, and introduced to electrochemical research. For the electrode system, a sine wave of AC voltage (current) signal produces a corresponding current (voltage) signals that can be characterized by the impedance or admittance of the electrode. Impedance spectrums generated by series of sine wave signals was named as electrochemical impedance spectroscopy.

A PVDF fiber mesh can be represented by an equivalent circuit as shown in Fig 12. When the electric signal frequency is low, such as 10 Hz, the impedance of the entire circuit is large, the electrical signal can not go through the capacitor C, only through the resistence R_2. Therefore the impedance of the circuit is R_1 plus R_2. Tipically, because the polymer doesn’t have charge carriers, such as free electrons, mobile ions or holes, it behaves an electrical insulator, or dielectric, and therefore resistence R_2 is very high giving a high impedance value. When the frequency increases to higher values, e.g. 1 MHz, the electrical signal can go through the capacitor C easier than through the resistence R_2. Therefore the impedance of the capacitor C dominates the circuit. and when an electrical signal was high enough to go through the capacitor C completely, corresponding impedance value was almost zero.

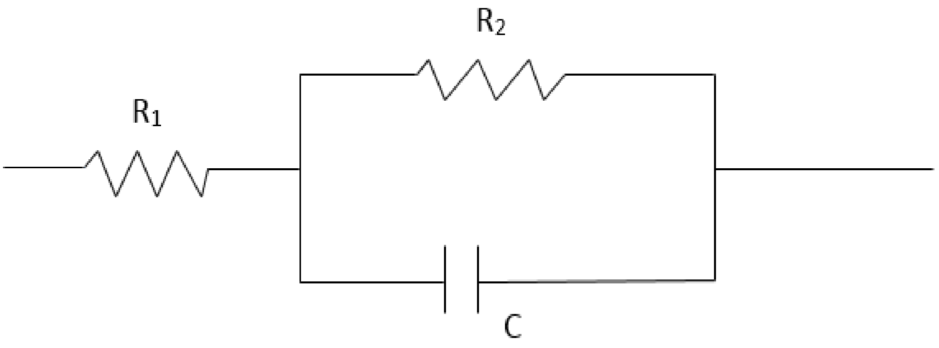

Fig. 12: Equivalent circuit model of PVDF fiber meshes.

The total impedance of the equivalent circuit, Z, is given by:

$$Z = Z_1 + \frac{Z_2 * Z_C}{Z_2 + Z_C} \text{ (2)}$$

Wherein, Z is the impedance of the entire circuit, Z_1 is the impedance of resistance R_1, Z_2 is the impedance of resistance R_2, Z_C is the impedance of the capacitor C.

The complex impedance of RC circuit is:

$$\mathrm{Z} = |\mathrm{Z}|\mathrm{e}^{-\mathrm{i}\theta} = R + iX \text{ (3)}$$

$$X = \frac{1}{z\pi f C_1} \text{ (4)}$$

Wherein, Z is he impedance of the entire circuit, f is the frequency of AC signal, ɵ is the phase angle of AC signal, C_1 is the capacity of the capacitor C;

So the mathematical model is:

$$\mathrm{Z} = |\mathrm{Z}|\mathrm{e}^{-\mathrm{i}\theta} = R + \mathrm{i}\frac{1}{z\pi f C_1} \text{ (5)}$$

Wherein, Z is the impedance of the entire circuit, R is the entire circuit's resistance, f is the frequency of AC signal, C_1 is the capacity of the capacitor C;

To be added, resistance is related to the material's length L and cross sectional area S by,

$$\mathrm{R} = \rho * \frac{L}{S} \text{ (6)}$$

$$\mathrm{R} = \frac{\rho}{t} \ \frac{L}{W} \text{ (7)}$$

Equation 7 indicated that resistance R was proportional to the length L, inversely proportional to the surface area S. When the fiber mesh had a certain thickness t, the resistance R is inversely proportional to the width W. At low frequency, resistance R dominates the impedance of the circuit. R is determined by three variables, which were resistivity (resistivity ρ was independent with the length and width of the fiber mat, regardless of shape), the length, surface area. The resistivity ρ can be assumed constant for the same PVDF fiber batch. As shown in Formula.8, the whole impedance changes with the shape of the fiber mats.

1.5.2 The progress in studing impedance of PVDF

The impedance of PVDF is very important for piezoelectric efficiency. When frequency is too high, the sensitivity of PVDF energy generator is very low[22-23]. Noémie Chocat[20] studied the impedance of P(VDF-TrFE) from 42 Hz to 5 MHz as shown in Fig 13. Z_{CPE} refers to the impedance of conductive electrode, $Z_{P(VDF-TrFE)}$ refers to the impedance of the piezoelectric layer of P(VDF-TrFE).

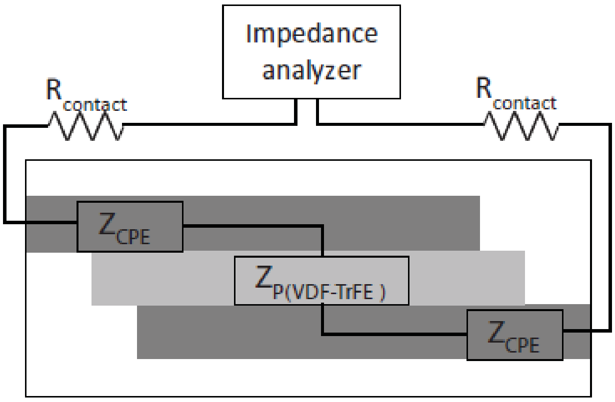

Fig. 13: Equivalent circuit model of a piezoelectric fiber connected to an impedance analyzer [20], where CPE represents constant phase element.

It was reported that the resistivity of the conductive electrode, which was conductive polymer, decreased with the electrical frequency f, when f was above a ciritical value f_0, this particular value f_0 was highly dependent on the preparation of electrode polymer So they observed the effect of f_0 for different samples on the resistivity of conductive el ectrode, and arrived at the following equation:

$$Z_{CPE}(f) = \frac{R_{CPE}}{1+j\frac{f}{f_0}} \quad (8)$$

Wherein R_{CPE} was the resistance under low frequency.less than f_0.

The impedance of P(VDF-TrEE) was caculated with the following equation:

$$Z_{P(VDF-TrFE)}(f) = \frac{1}{j\frac{\varepsilon_p S_p}{t_p}2\pi f} \quad (9)$$

$$\varepsilon_p = \varepsilon_p' + j\varepsilon_p'' \quad (10)$$

Wherein, S_p, t_p and ε_p refered to the effective surface area, the thickness, the dielectric constant of P(VDF-TrEE) relatively. The dielectric constant was a complex value with real and imaginary part, in this case it was treated as an constant.

The impedance of the system was equivalent to a function of the frequency f which gave an electrical model. As the electrodes were made with a conductive polymer, their impedance varies with frequency. The value of the resistor $R_{contact}$ is constant and does not change with frequency. So the whole impedance was given by the following equation:

$$Z_0(f) = 2R_{contact} + 2Z_{CPE}(f) + Z_{P(VDF-TrFE)}(f) \quad (11)$$

Fig. 14 shows the real and imaginary components, resistance and reactance, of a piezoelectric fiber with 3 cm, in which the real part is represented by the blue curve, the imaginary part represented by the red curve.

They tested a 3 cm long piezoelectric fiber and measured impedence spectrum. After fitting this model to measured data, they found $R_{contact}$was 4 kΩ, $R_{CPE}$was 58 kΩ, $f_0$was 890 kHz, $\varepsilon_p'$was 8.4 times ε_0, $\varepsilon_p''$was minus 0.12 times ε_0.

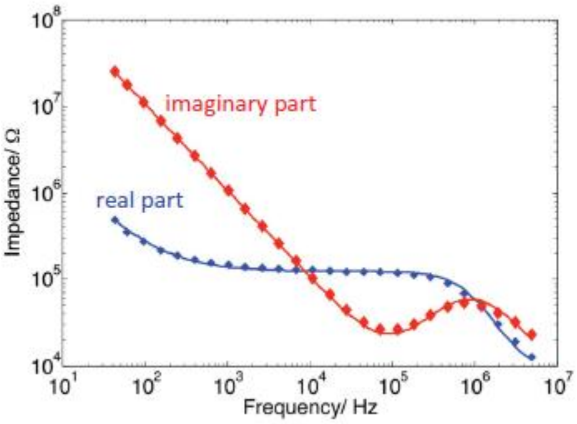

Fig. 14: Measured (diamonds) and simulated (solid line) electrical impedance real and imaginary parts[20].

Furthermore, this report said the values of ε'_p and ε''_p were fitted with references. It meant this model can be trusted. In conclusion, this research confirmed that the piezoelectric effect of P(VDF-TrEE) was affected by folded structure. By increasing effective area, the piezoelectric effect was improved. It made a theory and pratical foundation for large, flexible and adjusting acoustic emission and detection devices.

Darestani, D. T. et al[24] from University of Queensland, prepared PVDF piezoelectric film by poling PVDF extrusion uner intensively electrical filed and tested the impedance in a range between 0.01 to 100 000 Hz electrical frequency. In their paper, they set a different electrical model to investigate the small differences at low frequency, because they believed those differences contributed to the inverse piezoelectric effect. As we can see from Fig. 15, The vibration amplitude measured by a laser Doppler vibrometer at 5 Hz was shown when an electrical signal at 5 Hz was applied to the PVDF poled membrane. For comparison, the blue curve shown the response for PVDF un-poled membrane.

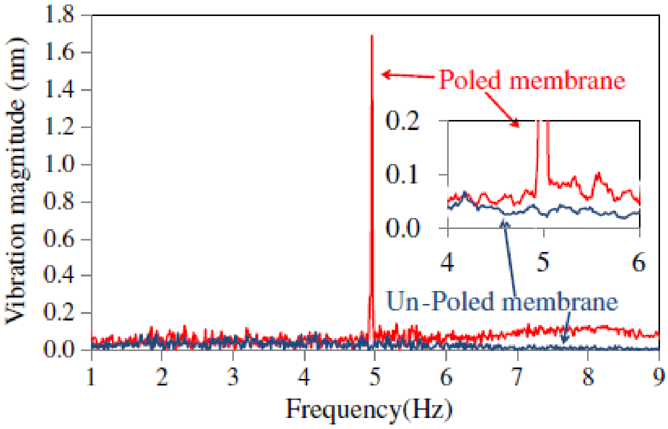

Fig. 15: The vibration amplitude at low frequency in PVDF poled and un-poled membrane [24].

Based on Fig. 13, Furthermore, the circuits model shown in Fig. 16 is to account for the low frequency behavior, they had to use an equivalent circuit model with four elements shown in (a), and the impedance spectrum of PVDF poled membrane is shown in (b). The numbers in (b) represented the elements numbers in (a).

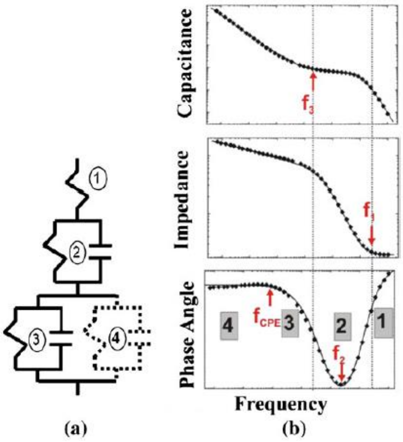

Fig. 16: (a) Circuit model and (b) impedance spectrum; the numbers are corresponded[24].

The results shown that, the experimental data measured in this report fitted with the model, and the impedance of the polar PVDF film was lower than the non-polar one. The constant phase angle at low frequency was caused by piezoelectric effect of polar PVDF film.

1.6 The biological applications of PVDF fibers

The great development of electrospinning technology facilitates its application in various fields, such as preparing biological tissue scaffolds. It partially mimics the structure and function of natural biological extracellular matrix (ECM), promoting cell attachment and growth, because of large space and specific surface area[25.26]. So far, there several natural or synthetic polymers were used for electrospining preparation of bioactive scaffolds, such as PAMMA, PLGA[27-32]. Some reports indicate that PVDF nanofibers can reduce shrinkage of scar tissue and greatly reduce granuloma formation (scar tissue) [33-35].

In a recent report[25], PVDF-TrEE scaffolds were prepared and cell compatibility was studied. This report pointed that PVDF-TrEE scaffolds have a great potential in tissue engineering applications. Guo et.al studied PU/PVDF composite scaffolds prepared by electrospinning. PU (polyurethane) were thermoplastic and elastic, it was widely used in the manufacturing of prosthesis[36-38]. PVDF was included in a composite with PU to increase the flexibility of the scaffold. The study characterized the PVDF crystalline phase, and the piezoelectric effect on fibroblasts cultures in vitro and in vivo. The application of this scaffold was for wound dressings. Wound healing refers to the process of wound repair in skin or other biological tissue. This process can be accelerated or facilitated by the wound dressing[39-42]. It also mentioned that electrical stimulation can affect cell behaviors, such as cell growth and reproduction, differentiation and regeneration. Previous studies[43-47] indicated that mechanical strain generated by electrical stimulation of piezoelectric materials may be used to prepare biologically active surfaces. To be mentioned, electrical stimulation can promote expression and secretion of growth factors, affect cells proliferation, differentiation and regeneration[48]. For example, electrospun scaffold in cardiac tissue engineering exhibited excellent advantages in promoting the formation and functionalization of cardiac tissue[49-51].

The cytotoxicity effect of PVDF fiber meshes on living cells reflects the biocompatibility, which is vital and fundamental in bio-engineering applications. There are several methods to evaluate the cytotoxicity. First, we can use chemical dyes, such as trypan blue to dye and mark some special structure in cells or cell membranes. Second, we can detect some metabolites' activity in cells to demonstrate cells' viability indirectly. Third is MTT, XTT or MTS assays, the most common method in biomedical experiments. These assays use resazurin as a reagent to dye enzymes produced by cells. As resazurin is a fluorescent dye and appears fluorescent color under infrared light, which can be used to investigate the cytotoxicity and cell viability. Resazurin is very sensitive, and the sensitivity reached 14 cells / well[25].

1.7 Innovation and objectives

Electrospinning tecnique has developed intensively and is commonly used to prepare PVDF nanofibers while, simultaneouslly, converting from α phase to β phase. Most of them were used to study direct piezoelectric effect of PVDF fibers as sensors[52-57]. These sensors have excellent flexibility and sensitivity. They are used for heart rate measurement, pulse sensors, energy harvest devices and so on[58-62]. Efforts also have been made on tissue engineering by tring to study the biocompatibility of PVDF nanofibers. However, judging from the different reports, the principles and parameters for preparation of PVDF electrospun nanofibers are not clear and uniform. The inverse piezoelectric effect of PVDF fibers has not been properly studied. Although PVDF nanofibers was regarded as untoxic either in vivo or in vitro , its biocompatibility is still not authorized by FDA (U.S. Food and Drug Administration).

The objectives of my project were to prepare PVDF nanofibers by electrospinning, and use them as active scaffolds for tissue engineering, using the piezoelectric generated mechanical strain, at low frequency, to stimulate and modify the cellular behavior, as listed below and depicted on Fig. 17.

1. Preparation of electrospun piezoelectric PVDF nanofibers.
2. Preparation of PVDF fiber mat assemblies on electrodes and test their electric properties.
3. Study of inverse piezoelectric actuation of nanofiber mat assemblies.
4. Test the biocompatibility of the PVDF nanofibers.
5. Study the effect of piezoelectric actuation on living cells.

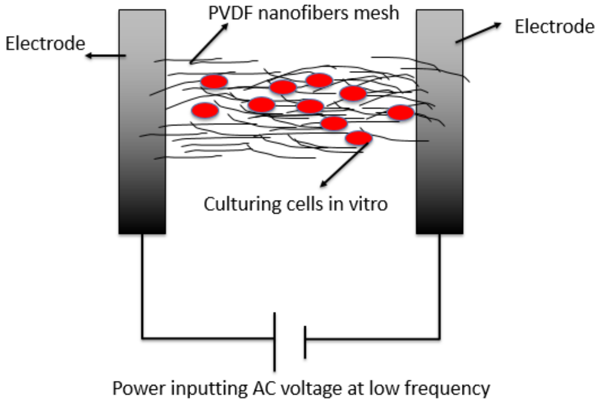

Fig. 17: Schematic of main objectives in this project.

In the first step we will use electrospinning to prepare PVDF nanofibers and study the effect of spinning parameters on the morphology and the ratio of β phase to α phase.

The second step is to prepare PVDF fiber mat assemblies on electrodes and study the impedance of PVDF nanofibers mesh in different geometric shapes and β phase ratios.

The third step is for confirming inverse piezoelectric effect at low electrical frequency.

Following the third step, the fourth one is to test cytotoxicity of PVDF fibers.

Only after confirming untotoxicity of PVDF fibers and inverse piezoelectric effect at low electrical frequency, the last step is to stimulate cells culturing by generating mechanical strain at low electrical frequency, which should not be harmful to the cells.

CHAPTER 2 – MATERIALS AND METHODS

2.1 Reagents and equipment

Most materials and instruments are listed in Table. 1 and Table. 2. NIH3T3 cells, which are mouse embryo fibroblasts, were obtained from sub-culturing. Cell culture petri dishes were purchased from Nunc, pipettes were obtained from GenicBio (Shanghai, China). Normal tools, like tweezers, knives, copper wires, glasses, were used for the experiments when needed. Beakers, measuring cylinders, stirrers with different specifications were washed by deionized water and dried in an oven. To be noticed, two different electrospinning apparatus were employed for preparing PVDF nanofibers. Apparatus 1 had some difficulties to adjust syringe pump, so spinning speed was considered invariant. Apparatus 2 was used to investigate the effect of the spinning speed to morphology and crystalline phase of PVDF nanofibers.

Table. 1: Materials.

Name	Specification	Seller
Polyvinylidene Fluoride (PVDF)	FR904，Mw=600.000	Sigma
N,N-dimethyl formamide (DMF)	Analytical	Sigma
Acetone	Analytical	Sigma
Electric conductive ink	Commercial	Bare Conductive Ltd
Dulbecco’s phosphate buffered saline	D5773-50L	Sigma
Resazurin	30025-1	Biotium

Table. 2: Instruments.

Instrument	Type	Seller
Electrospinning apparatus 1 (Belong to Madeira University)	FM1108-Electrospinning System	Beijing Future Material Sci-tech Co.Ltd
Electrospinning apparatus 2 (Belong to Wuhan Textile University)	SS-3556H	Beijing Ucalery tech Co.Ltd
Electronic analytical balance	ME204E	Mettler Toledo
Magnetic stirring apparatus	MR 3001	Heidolph
Rotational rheometer	Kinexus	Malvern Instruments Ltd
Scanning electron microscope	JSM-6510	JEOL Ltd
Fourier transform infrared spectrometer (ATR)	FTIR 4200	Perkin Elmer
Laminar flow hood	Class II A/B3	NUAIRE
Incubator	Autoflow IR Direct Heat CO2	NUAIRE
Inverted optical microscopy	CK40	OLYMPUS
Microplate reader	VICTOR3™	PerkinElmer
Tissue culture test plates	Gamma sterilized	Orange Scientific

2.2 Electrospinning PVDF fibers

DMF and acetone were mixed in volume ratios 6/4 and 8/2, respectively, to prepare 10 mL solvent mixture samples. Then 0.2 g, 0.4 g, 0.6 g, 0.8 g, 1.0 g, 1.2 g, 1.4 g, 1.6 g, 1.8 g, 2.0 g PVDF powder samples were weighed precisely with an electronic analytical balance. The PVDF samples were added to the two different solvent mixtures, independently and separately, to be dissolved by magnetic stirring for 24 h. The result was the preparation of PVDF polymer solutions with mass-volume concentrations ranging from 2% to 20%, with intervals of 2% concentration. Spinning voltage was set from 18 kV to 32 kV; collector distance was always 15 cm; the rotating collector's speed was controlled with an electric motor, between 0 and 300 rpm, to obtain fibers with different orientations; spinning speeds were set with polymer liquid solutions flowing at 0.5 ml/h, 1.0 ml/h, 1.5 ml/h, 2.0 ml/h, 3.0 ml/h, using a digitally controlled injection syringe pump; diameters of metal needle tips were 0.5, 0.8, 0.9 and 1.2 mm. Temperature and humidity inside the spinning chamber were maintained within 28 to 30 ℃ and 40% to 50%, respectively.

Table. 3: Parameters of electrospinning processing.

Parameters	Values
Polymer concentration (wt%)	0, 2, 4, 6, 8, 10, 12, 14, 16, 18, 20
Applied voltage (kV)	18 to 32
Needle diameter (mm)	0.5, 0.8, 0.9, 1.2
Spinning speed (ml/h)	0.5, 1.0, 1.5, 2.0
Rotating speed (rpm)	0, 100, 200, 300

During the whole processing the needle-to-collector distance was always 15 cm, this condition maintained constant regardless the variation of other parameters studied. An aluminium foil covered plate (length: 20 cm; width: 10 cm) or rotating cylinder (diameter: 8 cm; length: 20 cm; rotating speed: 0-300 rpm) were used for the nanofiber collection target. The thickness of fiber meshes were controlled by the same deposition time of the spinning process which was 1 hour. The whole processing was conducted at constant temperature and humidity. All the electrospun PVDF nanofiber meshes were then put in an oven to be dried at 40 °C for 2 hours, to evaporate the residual solvent, and after that all nanofiber meshes were removed gently from the surface of the aluminium foil with tweezers; at last, these nanofiber mesh samples were classified and labeled carefully for next steps.

2.3 Preparation of PVDF fibers electroactuator

To be noticed, electrical conductive ink was used as for preparation of electrodes on the glass plates. The conductive ink was chosen as an easy and cheap alternative to gold or silver sputtering, for which we didn’t have the appropriate equipment. The viscous conductive ink is water based and its exact composition is a commercial secret. A secondary objective, for using the conductive ink, was the future prospect of using inkjet printing for the electrode material deposition, directly on the polymer fiber mats.

First, the conductive ink was applied on 76 by 26 mm glass slides and allowed to dry; then we cut them into strip electrodes with 1, 2, 4,or 8 mm spacing; the width of the strip electrodes was 5 mm, thickness was estimated to be constant. The electrodes were completed with thin copper wires, bonded to the ink strips with more conductive ink. These electrodes were used as substrates of the PVDF fiber mats. The contact between the fibers and the electrodes was done with a thin layer of fresh conductive ink, covered on top in order to enhance the connection and reduce contact resistance. Fig.18 (a). and Fig.18 (b) shows the two possible structures of PVDF fiber electroactuator. Fiber mesh was suspended between the conductive electrodes.

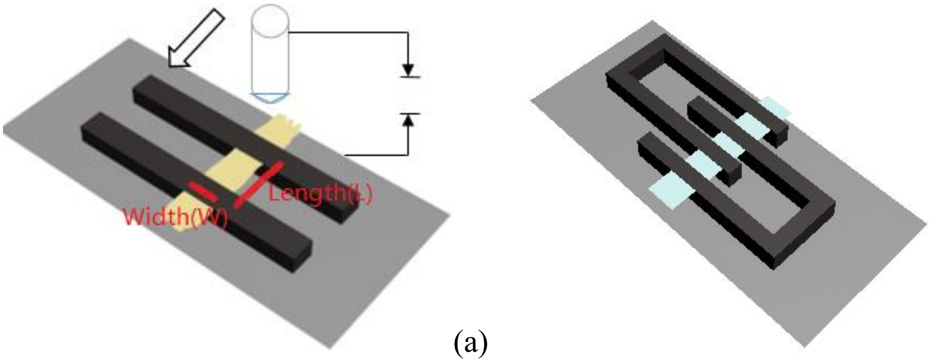

(a) (b)

Fig. 18: (a) and (b) 3D modeling photos in different geometric structure of PVDF electroactuator.

All the PVDF fiber meshes were prepared in the optimal condition with finest and most uniform morphology which meant the highest β/α phase ratio, as demonstrated in last chapter.

After preparing 1, 2, 4, 8 mm spacing folded conductive electrode substrate, we sticked the 1x11, 12x2, 14x5, 18x10 mm sizes of PVDF fiber meshes on the surface of the electrodes in such way that the fibers' The orientation should be perpendicular to the parallel direction of the electrode. At last a uniform layer of conductive ink was used to guarantee a gppd contact between the fibers and the electrodes and waited to be dried completely. The specific parameters were in the table. 4.

Table. 4: Parameters of PVDF fiber electroactuator geometry: length (L) and width (W).

L（mm）	W(mm)
1	10
2	10
4	10
8	10

By the same way, we sticked the 11x1, 11x2, 11x5,11X10 mm sizes of PVDF fiber meshes on the surface of substrate with 1 mm spacing electrode. The other operation was the same. The specific parameters are in the table. 5.

Table. 5: Parameters of PVDF film electroactuator geometry: length (L) and width (W).

L（mm）	W(mm)
1	1
1	2
1	5
1	10

The real PVDF electroactuator samples are shown in Fig.19, which adopt the structure in Fig. 18 (b).

Fig. 19: The real photo of PVDF electroactuator.

2.4 Electrical modeling for PVDF electroactuator

According to the Formula 5, we set up an equivalent circuit model. In this model, at low electrical signal frequency, such as 10 Hz, the impedance of the entire circuit was very high. At such low frequency, the electrical signal can not go through capacitor C, and therefore the impedance of the circuit was dominated by resistance R_2; When the frequency increased to 100 kHz, the electrical signal can easily go through the capacitor C, thus the impedance of the circuit was zero.

2.5 Preparation for cells cytotoxicity

To investigate cytotoxicity of PVDF fibers, we prepared three kinds of fiber meshes, with different compositions: PVDF, PVDF/PLGA and PLGA. However, the fiber meshes were very difficult to be put inside the wells for cell culturing, one PVDF sample was damaged during experiments. PLGA samples was dissolved in acetone when we were sterilizing them. After several times, all samples were prepared successfully. The fiber meshes were cut into 2 cm * 2 cm size squares, maintaining uniform thickness. The whole procedure was completed in bioclean environment. Every group had four repeated samples except for PVDF, so we just chose three repeated data for each sampel. All fiber samples were put on the surface of 1.5 cm diameter round and thin glass, then folded by tweezers to cover the entire glass. The surface on the top of fiber meshes should be smooth and flat.

Under sterile conditions, all the samples were put into petri dishes with 70% volume concentration of ethanol for 5 min, then immersed in PBS solution for half hour to remove residual ethanol. After twice repetition, the samples were put into 24*6 wells culture plates, carefully to make sure they fitted in the bottom of the wells. The culture wells plate was marked as indicated in Table.6.

Table. 6: Different samples in culture wells plate.

Control	PVDF	PLGA/PVDF	PLGA
A01	B01	C01	D01
A02	B02	C02	D02
A03	B03	C03	D03

The NIH/3T3 cells, which named by mouse fibroblasts cell line in cells culturing, were cultured in culture medium and were maintained at 37 ˚C, 5% CO_2 in cell culture petri dish, waiting for inoculation. The culture medium was refreshed every 2 days. Meanwhile we placed the cells culture petri dish under the microscope at 10,000 magnifications to observe the cells morphology and make sure the cells were alive. Then we removed the culture medium and added 1 mL PBS to wash. After several times, we removed all PBS and added 1 mL trypsin, then the petri dish was put back into the incubator for 5 minutes. After adding another 1 mL culture medium, we took 20 μL solution and diluted them into 100 μL. A small amount of dilution was added on the slide, and observed under the optical microscope for cell counting, which allowed us to estimate the total number of cells. Finally, 1 mL of cell culture was added to each previously prepared well, immersing the fiber samples; each culture well received approximately 50000 cells. The culture plate was put in the incubator with labels for 1 and 3 days respectively.

At last, we prepared 10% resazurin solution by adding 800 μL of resazurin and 7.2 mL of culture medium respectively. After 1 day, each well was added 500 μL of resazurin solution and put back into incubator for 3 h.

2.6 Characterization

In the electrospinning process, the viscosity and rheological properties of the spinning solution has a great influence on the fiber forming and morphology. Before preparation of PVDF fiber meshes, PVDF spinning solutions with different concentrations were tested by Kinexus rheometer to characterize rheological properties and characteristic viscosity. To be more specific, different PVDF solutions were coated onto a fitted metal plate in the rotational rheometer (Kinexus, Malvern Instruments Ltd). Related and characteristic viscosities were recorded automatically under shear stress from 0 Pa to 120 Pa and shear rate from 0.10 s^{-1} to 100 s^{-1} at room temperature 25 °C. We also tested solvent viscosity and defined it as η_S. After collecting raw data, we calculated relative viscosity by the formula:

$$\eta_{sp} = \frac{\eta_0 - \eta_S}{\eta_S} \qquad (12)^{17}$$

Wherein η_0 refers to zero-shear viscosity which were obtained from raw data at Newtonian region; η_S represents the pure solvent viscosity; η_{sp} is the specific viscosity which physically characterizes the effect of the polymer on the solution viscosity.

After electrospinning all the nanofiber mesh samples, small cuts were separated for scanning electron microscopy testing. The small cuts were stacked on the surface of carbon conductive paste, then coated with gold powder by JFC 1600 auto fine coater to increase conductivity so that electrons can impinge samples easily. Using the model JSM-6510 scanning electron microscope, the fibers' morphology was observed. The acceleration voltage of the SEM system was 15 KV. Fiber diameter was measured through image processing software (ImageJ).

FTIR was used to confirm the PVDF composition and also to estimate the β/α phase ratio. Spectra were acquired in a FTIR-4200 Fourier transform infrared spectrometer using both the transmittance and ATR (Attenuated Total. Reflectance) techniques. The α, β crystal phase peaks and the β/α phase ratios were investigated in

PVDF fibers prepared under different conditions. FTIR-ATR apparatus revealed to be suitable for powder and fibrous samples, sample preparation is simple and easy to operate, test process is fast and results are reliable.

The impedance characterization of the fibers-on-electrodes assemblies was done with an electrochemical workstation, PARSTAT 2263 Advanced Electrichemical System.

At last, a MTT assay was conducted to evaluate the viability of NIH3T3 cells in PVDF fiber meshes. Microplate reader (PerkinElmer VICTOR3™) was used to analysis the cells viability.

2.7 Computational modeling

In order to understand the differences between α and β phase PVDF, as well as the mechanism behind the transition from α to β, we performed several molecular modeling studies. Single short polymer chains with 8, 16 and 64 monomer units were separately built, in both perfect α and β conformations. All molecules were geometrically optimized with the PM3 semiempirical quantum mechanics method, as implemented in *HyperChem 8.010 for Windows*. The shorter chains, with just 8 monomer units, were also optimized with ab initio quantum mechanics, using a simple 6-31G* basis set, as implemented in *Spartan 1.1.4*. All simulations were performed on a Windows based laptop with an Intel Core i5-2410M CPU at 2.30 GHz. The quantum mechanics allowed the energy and atomic point charge calculations, which are essential for the response to the external electric field, but even the semiempirical method is too slow for a useful molecular dynamics implementation with multiple polymer chains. Therefore, for the molecular dynamics (MD) study under an external electric field, the AMBER99 force field was the choice and software used was *HyperChem 8.010 for Windows*.

HyperChem allows the implementations of several calculations methods with application of an external static electric field. The software's electric field orientation and intensity can be user defined, but its intensity is given in arbitrary units. For the purpose of our study, a simple method using the acceleration of a test charge allowed us to find a conversion factor from those arbitrary units to a more convenient SI unit of volt per meter.

Because the atomic point charges calculated with the PM3 method are very dependent on the conformation and would not be valid throughout the MD study, we decided to use the *Gasteiger-Marsili* algorithm[63] to calculate fixed atomic point charges. The implementation of *Gasteiger*'s *partial equalization of orbital electronegativities* was done in Microsoft Excel with our own code written in Visual Basic (VBA).

For the MD study, two α type, 64 monomer units long, polymer chains with *Gasteiger* charges were duplicated and allowed to equilibrate in vacuum at a temperature of 500 K for 500 ps and then at 100 K for the same period. This resulted in a *ball* shaped particle with an approximate diameter of 3 nm and roughly 17% β type units. Further MD simulations were performed at 100 K for a 200 ps period, with different values of external electric field. For each simulation run, the number of monomer units with the α or β conformation was recorded and used to estimate the β/α ratio of the sample. Further simulation details and results will be discussed under chapter 3.

CHAPTER 3 – RESULTS AND DISCUSSION

3.1 The effect of solvent composition on fiber morphology

Since the polymer solution's solvent can affect the electrospinning process, we tested two different mixtures of DMF and acetone with volume ratios, respectively 8:2 and 6:4. The morphology of the electrospun fibers was observed with SEM as can be seen in Fig. 20. We concluded that when the DMF/acetone volume ratio was 8:2, the lower acetone content resulted on lower volatility in the jet, leading to traces of solvent in the deposited fibers and the formation of relatively large polymer droplets. When the DMF/acetone volume ratio was 6:4, the fiber droplets disappeared, the spinning process was more continuous and the PVDF fiber meshes were easily prepared. So we chose 6:4 as DMF/acetone volume ratio for subsequent experiments. Although we didn't do any experimental verification, we can reasonably speculate that excess acetone would result on faster solvent evaporation and formation of fibers with larger diameter, which would not be desirable.

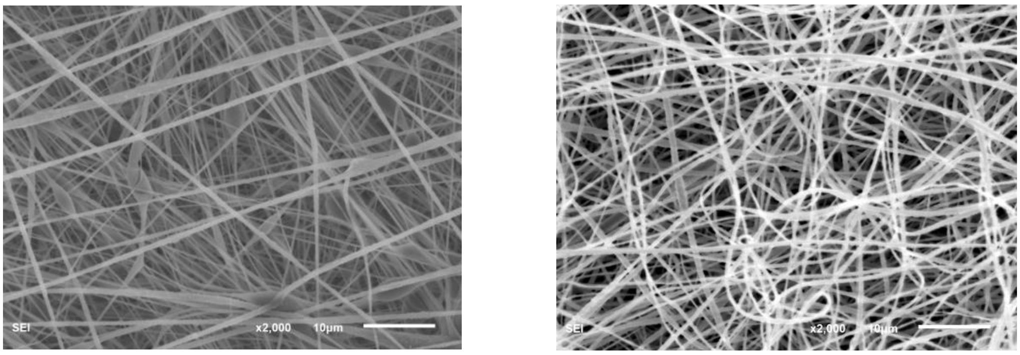

(a) (b)

Fig. 20: SEM images of PVDF fibers produced with different solvent volume ratios of DMF and Acetone: (a) 8:2; (b) 6:4. The polymer composition is the same 12 wt %.

3.2 Rheological properties of spinning solutions

To investigate the effect of the polymer solution's intrinsic properties on morphology of electrospun fibers, we prepared a series of solutions with different concentrations and manufactured the corresponding nanofiber meshes under constant external conditions, like applied voltage, needle diameters and collecting distance.

Generally, from the viewpoint of materials' properties, the polymer solution's viscosity is considered the most important parameter in the formation of electrospun fibers. We can explain the effect of viscosity properties of polymer solutions on the electrospinning process, by using polymer chains entanglement[17]. In this molecular model, there exists a critical concentration which dictates the electrospinning behavior of the solution, i.e. the polymer solution must have concentration higher than the critical value. First, when the solution concentration is lower than the critical concentration, it means polymer chains are not entangled enough and solution is too dilute for proper electrospinning and formation of nanofibers will be unsuccessful. Second, when the solution concentration is close to the critical concentration, which is called semi-entangled state, there is a higher probability to form nanofibers in the process of electrospinning. But if the polymer chains are not sufficiently entangled, it is easy to form some beads or droplets. Third, when the solution concentration is higher than the critical concentration, polymer chains are sufficiently entangled and this is called concentrated state. In this regime, the successful formation of nanofibers is much easier, without obvious beads. However, there is also a limited concentration range, because when polymer chains are far way entangled, it is very hard to stretch them and form fibers, which means the solution will not be able to cast a jet and thus the electrospinning is impossible.

Zero-shear viscosity and specific viscosity were measured for several PVDF polymer solutions and listed in Table. 7.

Table. 7: Characteristic viscosities in different concentrations of PVDF.

wt%	$\eta_0(mPa \cdot s)$	$\eta_{sp}(mPa \cdot s)$
2	3.414	2.021
4	12.94	10.45
6	34.39	29.43
8	79.36	69.23
10	176	154.75
12	248	218.47
14	478	422.01
16	793	700.77
18	1566	1384.84
20	2708	2395.46

We plotted the specific viscosity against polymer solution concentration in Fig. 21 and defined the critical concentration as 8 wt%. The plot was divided in three areas corresponding to the untangled state, semi-entangled state, and concentrated state.

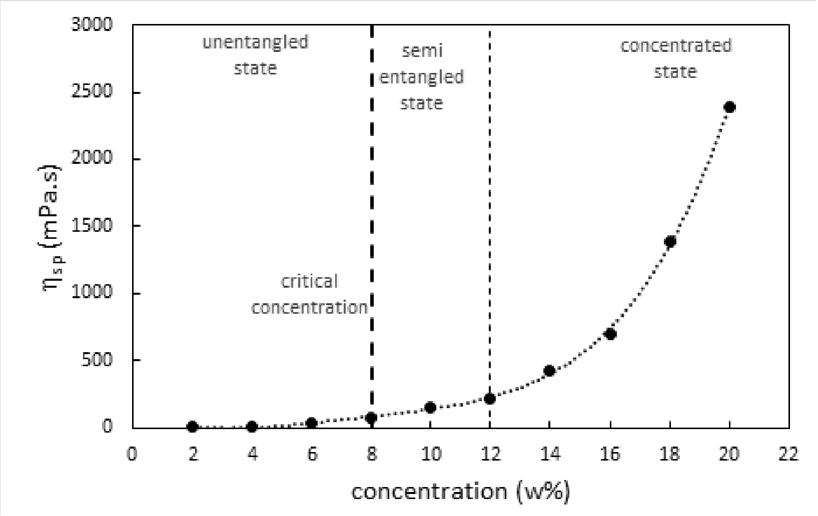

Fig. 21: Trending curve of characteristic viscosity in different concentrations of PVDF solutions.

Fig. 22 depict typical SEM images of electrospun PVDF nanofibers at different polymer concentrations. The alignment of the individual fibers is random and a fibrous morphology with different sizes is observable.

We found that, when the polymer concentration was below the critical value of 8 wt%, neither fibers nor beads were obtained, since the solution was too dilute and the polymer chains were in the untangled state. When the polymer concentration went above the critical concentration, the electrospinning process generated obvious beads along with the fibers. This effect is different from the one observed with the solvent's volatility and, in this case, according to the polymer chain entanglement model, the solution exhibits the semi-entangled state and the low viscosity, which, associated to the high surface tension, favors the formation of beads and the polymer chains do not stretch completely under the applied electric field.

When the polymer concentration increased to 10 wt%, we could observe that the beads started to disappear from the fiber mesh. In this case the balance between high viscosity and not so high surface tension allow the polymer jet to stretch under the electric force, leading to better formed fibers. Nevertheless, the semi-entangled state still allowed some bead formation.

Once the polymer solution reached 12 wt%, we could consider that the concentrated state, or entangled state, had been achieved, since the SEM images no longer show beads and the fibers were more uniform. This is the adequate regime for electrospinning, provided the viscosity doesn't become too high, in which case the fluid flow in the needle becomes too difficult. The fiber morphology observed in the SEM images confirm the entanglement model description.

From our experiments we concluded that there is an optimal range of polymer solution concentrations with a significant effect on nanofiber formation, not only on avoiding the formation of beads, but also regarding nanofiber thickness. The formation of nanofibers requires the polymer jet to stretch under the electric force, still as a solution. As the polymer concentration increases well above the critical value, in the concentrated state, the higher viscosity and solvent evaporation rate both contribute to slow down the stretching and speed up the solidification, which prevents the fibers from stretching and leads to larger average thickness. In our case, we wanted to obtain an average thickness of electrospun fibers under 1000 nm, because of potential advantage for electrical and biological engineering applications. As can be seen from the SEM images, at 12 wt%, our fibers exhibited quite homogenous thickness, below 500 nm. At 8 and 10 wt% the fibers' thickness was more disperse and beads larger than 1 μm was common. In following experiments, we always choose 12 wt% as experimental concentrations.

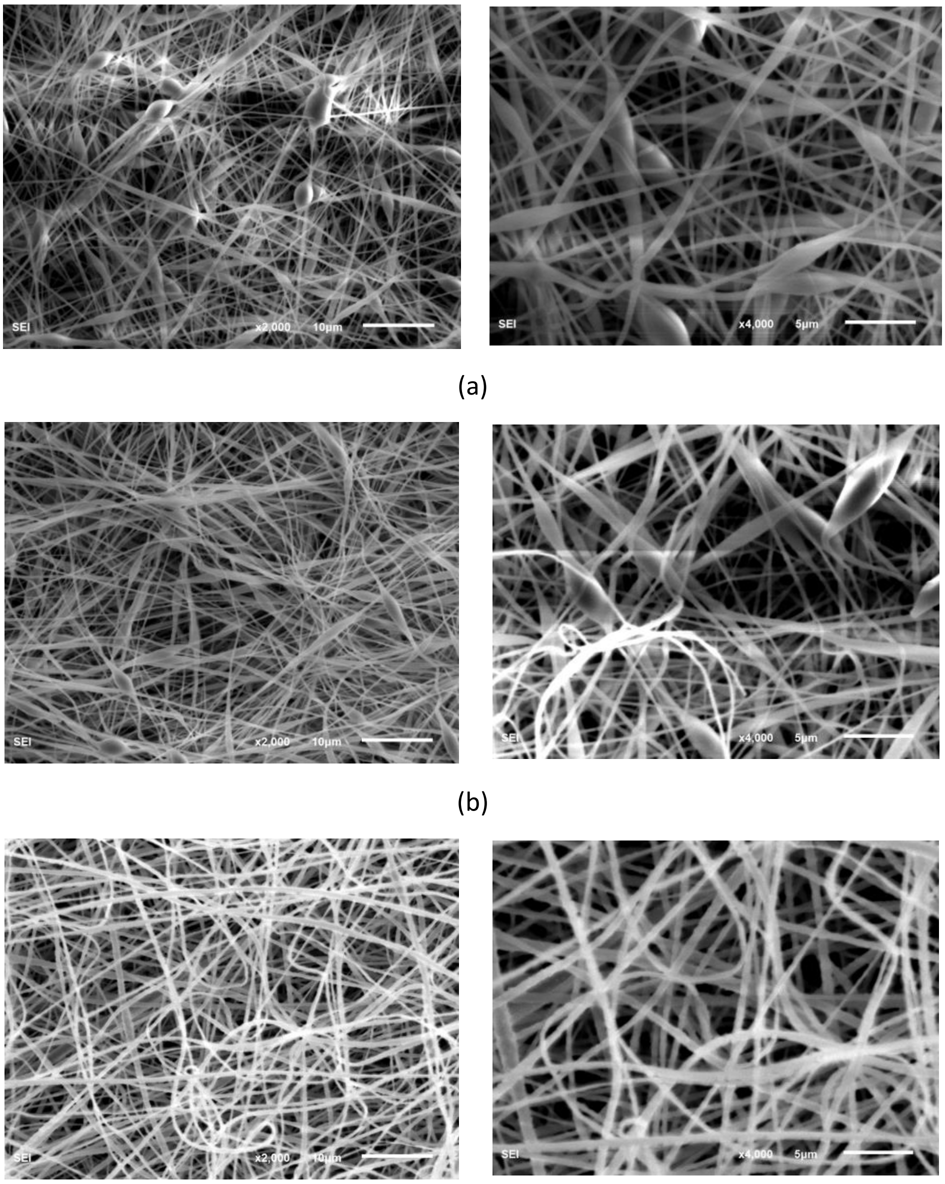

(a)

(b)

(c)

Fig. 22: PVDF SEM photos at 2000x (left) and 4000x (right) magnification factors: (a) 8 wt%, (b) 10 wt%, (c) 12 wt%.

3.3 The effect of applied voltage on fiber morphology

Adding to the effect of the polymer solution's intrinsic properties, the electrical field also has a significant effect on the formation of electrospun fibers including amount of beads and distribution of fibers. In the electrospinning process the electrical force drives the jet drops out of the needle and stretches them into fine fibers. In order to study on the effect of the applied voltage on the PVDF electrospinning, we set up a series of voltage values, keeping all the other parameters constant, like flow rate, needle diameter and solution concentration. We selected 12 wt% as an optimal concentration, 1.2 mm as needle diameter and 1.0 ml/has flow rate. Applied voltage was set up from 18 kV to 28 kV. From Fig. 23 we can see that the uniformity of the fibers improved upon increasing the applied voltage until 28 kV.

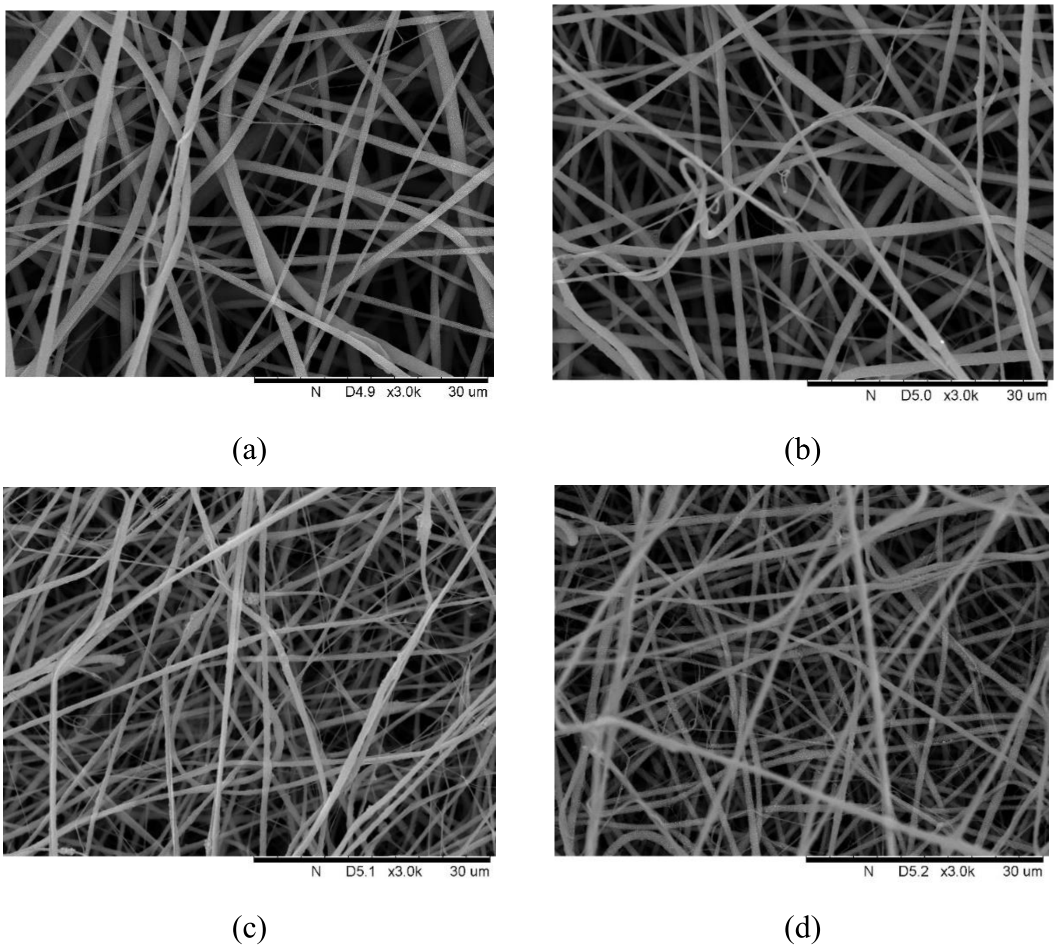

(a) (b)

(c) (d)

Fig. 23: 12 wt% PVDF SEM photos at different voltages: (a) 18 kV; (b) 21 kV; (c) 24 kV; (d) in 28 kV.

From 18 kV to 24 kV there was not enough stretching and most fibers are in the μm range When voltage increased from 24 kV to 28 kV, distribution of fibers was more uniform and most fibers were below 1 μm. At 28 kV the fibers were the finest and most uniform. However, when the applied voltage was much higher than 28 kV, we could not fabricate fiber or the fibers were coarse and with a bad distribution. One possible explanation is that when voltage was too high, the electrostatic force accelerated the jet too much, causing the flight duration to be too short and thus preventing the appropriate stretching of the fibers.

3.4 The effect of needle diameter on fiber morphology

Under the same operational conditions when we changed needle diameter the morphology of nanofibers also changed. We chose 0.5 mm, 0.8 mm, 0.9 mm and 1.2 mm needle diameters as variable factors. Applied voltage was set to 28 kV. For 0.8 mm, 0.9 mm, and 1.2 mm diameter needles, 1.0 ml/h flow rate was set. While for 0.5 mm diameter needle, flow rate was set to 2.0 ml/h because of spinning ability. From the SEM images in Fig. 24, we found that when needle diameter was 0.5 mm, fibers were crooked and stacked into each other due to the slower jet flow. At higher needle diameters, the fiber morphology improves, especially when the needle diameter was 0.9 mm and 1.2 mm. The surface area of the Taylor cone depends on the needle diameter. Under the electrical field, narrower needles may lead to higher electric field density at the tip of the Taylor cone, resulting in stronger electric force and acceleration of the jet. The short duration flight ultimately results in poor stretching of the fibers. At needle diameters of 0.9 mm and 1.2 mm, the polymer jet was able to stretch which resulted in fine and uniform fibers. When needle diameter was 1.2 mm, under 28 kV applied voltage and 1.0 ml/h flow rate, the morphology of fibers was the best.

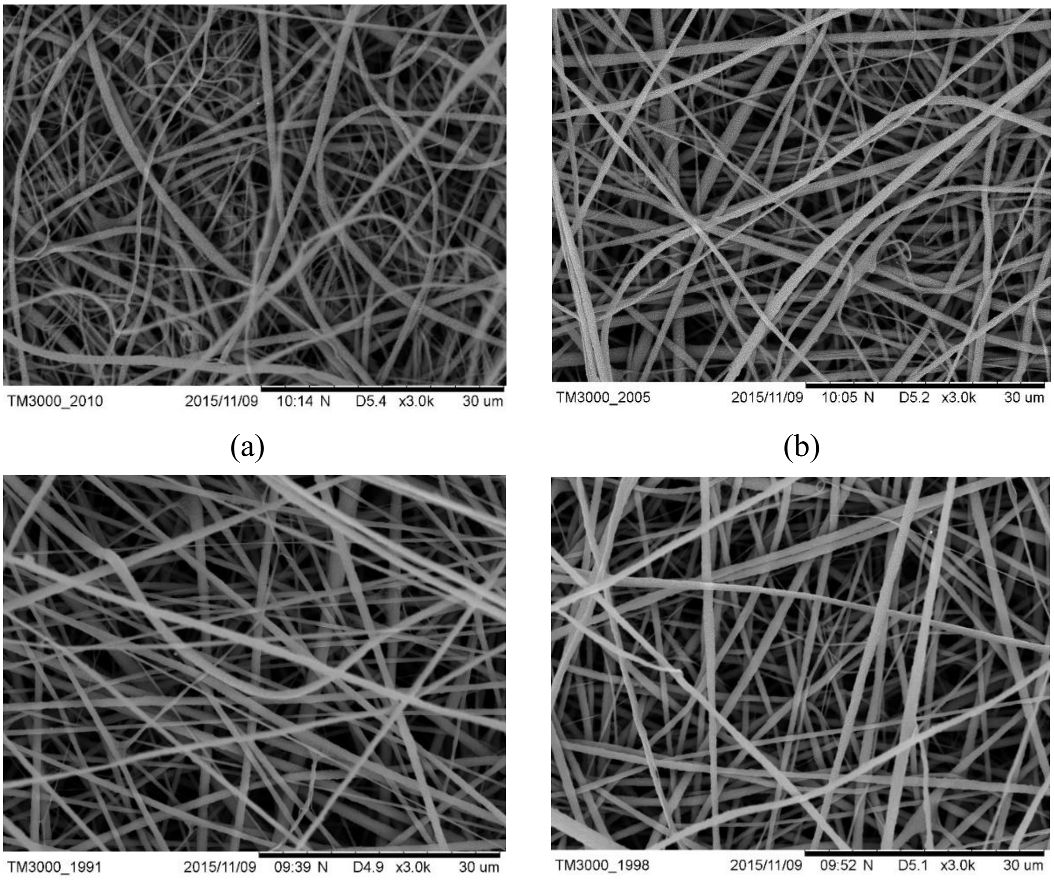

(a) (b)

(c) (d)

Fig. 24: PVDF SEM photos of fibers obtained with different needle diameters: (a) 0.5 mm; (b) 0.8 mm; (c) 0.9 mm; (d) 1.2 mm.

3.5 The effect of solution flow rate on fiber morphology

The polymer solution flow rate, or spinning speed, is known can also affect the fiber morphology. To test the best conditions, we did experiments with spinning speeds of 0.5, 1.0, 1.5 and 2.0 mL/h. We selected 12 wt% as optimal concentrations, 1.2 mm as needle diameter. Applied voltage was set up from as 28 kV, rotating speed was 0. As we can see from Fig. 25, at lower spinning speed fibers got more stretched, like in image (b) fibers were more straight and uniform without obvious drops and less crimp; but in image (a) there were some drops and not very uniform. When the spinning speed was higher, fibers became less uniform and more twisted, like in images (c); image (d) shows an even worse scenario with big curves, which means fiber didn't get stretched enough. The fiber production at 1.0 ml/h was better, and we got very nice fiber mats, better than with 0.5 ml/h flow, which lead us to choose 1.0 ml/h as the optimum spinning speed. As shown in image (b), the optimal condition was 1.0 ml/h spinning speed, 28 kV, 12 wt% polymer concentration which came from Fig. 25 (d).

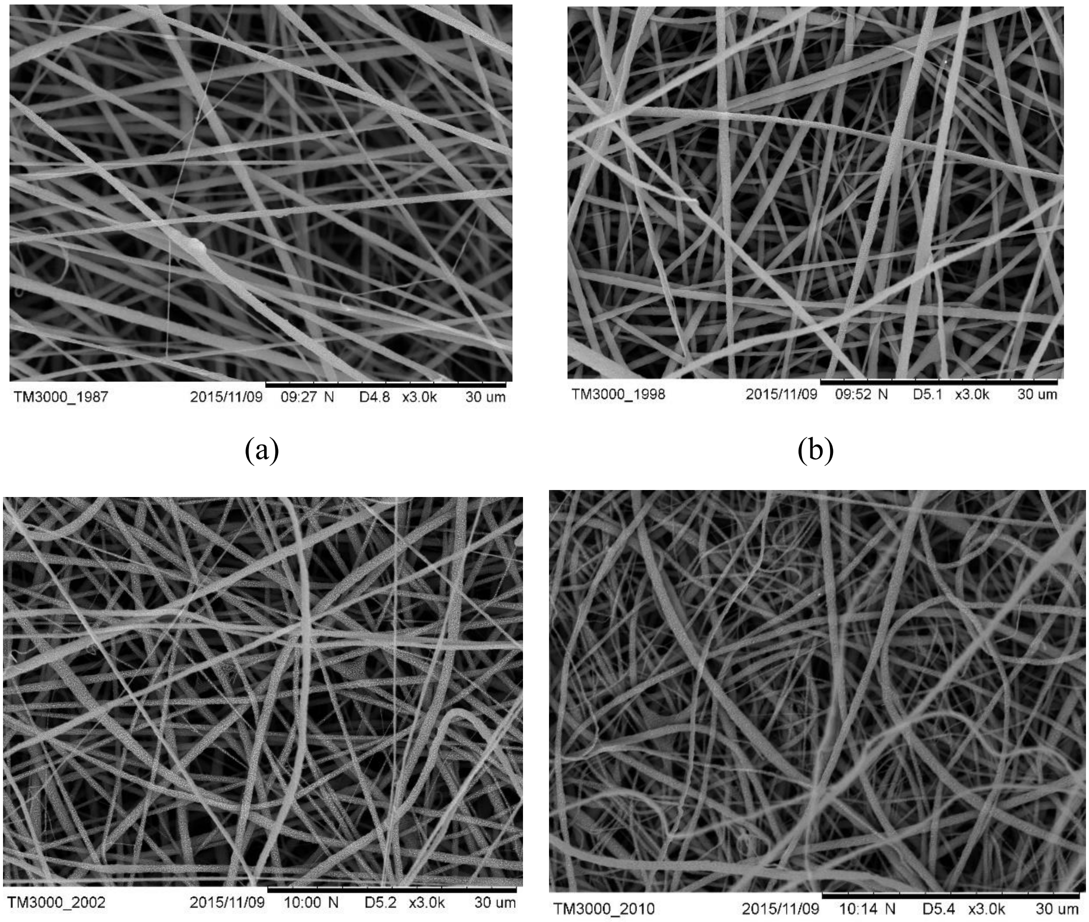

(a) (b)

(c) (d)

Fig. 25: SEM images by changing spinning speed from 0.5ml/h to 2.0ml/h with 0.5ml/h interval. (a), (b), (c), (d) are represented by fiber meshes fabricated in spinning speed 0.5ml/h, 1.0ml/h, 1.5ml/h, 2.0ml/h respectively.

3.6 The effect of collector rotating speed on fiber morphology

With a typical static collector, electrospun fibers don’t show a preferred orientation, in other words, the fiber mesh is made of randomly oriented fibers, as a result of the whipping effect of the electric field at the end of the flight. With a look on potential applications of the PVDF fibers, we intended to produce a fiber mesh with a preferred orientation. Our goal was to enhance the piezoelectric effect along the specific fiber orientation. For that purpose, we used a rotating metallic cylinder as collector, which is known to produce fiber meshes oriented perpendicularly to the axis of rotation. We can see from Fig. 26 that the collector's rotation had a positive effect on fibers alignment. These fibers were produced with optimal parameters. Polymer concentration was 12 wt%, needle diameter was 1.2 mm, applied voltage was 28 kV, and solution flow rate was 1.0 ml/h. When we set a plate with zero rotating speed, the collected fibers were randomly aligned in different directions like in image (a). While we increased rotating speed most of fibers were aligned in one direction, like in image (b), taken from fiber produced with the rotating speed of 300 rpm. The rotation, perpendicular to polymer jet, induces asymmetry in the electric field close to the collector and forces the fibers to wound around the cylinder. The whipping effect still creates some randomness, but the great majority of fibers follows a preferred orientation. The additional tangential velocity adds to the electric field acceleration, with a pulling effect, which helps the fiber stretching and a final morphology.

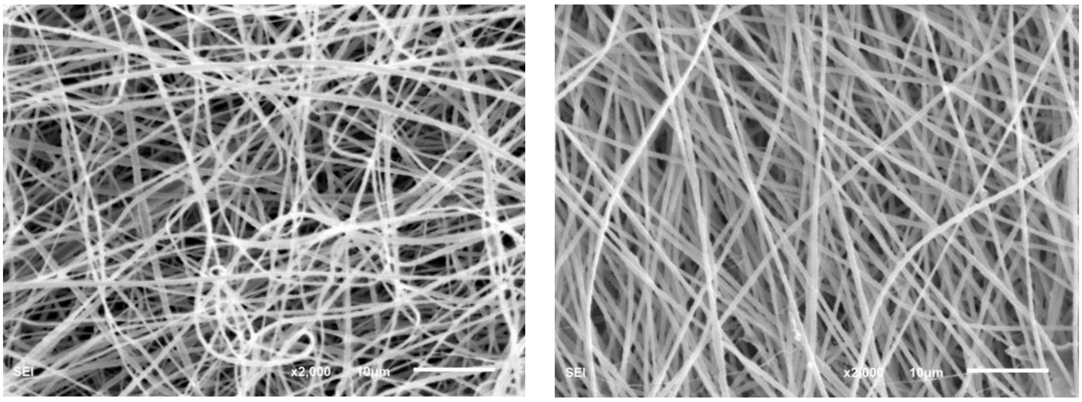

(a) (b)

Fig. 26: SEM images in (a) no rotating speed and (b) 300 rpm rotating speed.

3.7 The effect of polymer concentration on crystal phase structure

Fig. 27 shows the Fourier Transform Infrared (FTIR) spectra of the PVDF nanofibers produced from polymer solutions with different concentrations. As we can see from the spectrum plots, characteristic peaks at 765 cm^{-1} and 841 cm^{-1}, represent the existence of α and β phase, respectively. From the absorption data we calculated the β ratio (%) in the fibers, plotted in Fig. 28 against solution concentration. We can see that the β phase ratio increased with concentration reaching a maximum around 12 wt%, with the highest ratio at 83.80% According to these results, the β phase ratio could not be improved to 100% with increasing polymer solution concentration by electrospinning. A possible explanation is that when the solution concentration was too high, well above the semi-entangled regime, the viscosity was also very large, due to the intensively entangled polymer chains, reducing molecular mobility. This makes it very hard for the torsional angles to realign under the electric field, similarly to the fiber stretching mechanism.

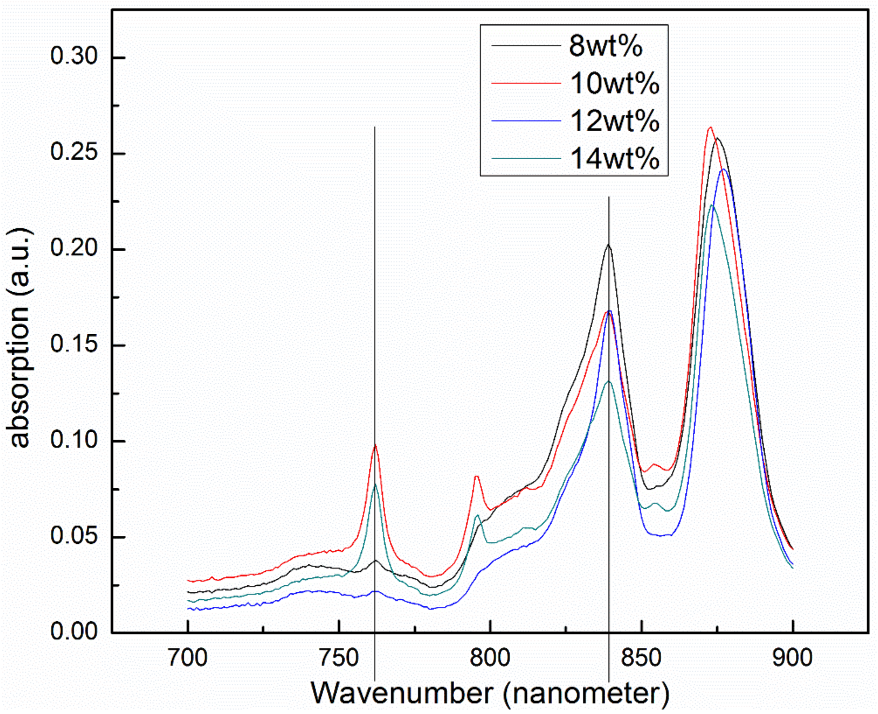

Fig. 27: FTIR-ATR spectrum of PVDF in concentration of 8 %, 10 %, 12 %, 14 wt%.

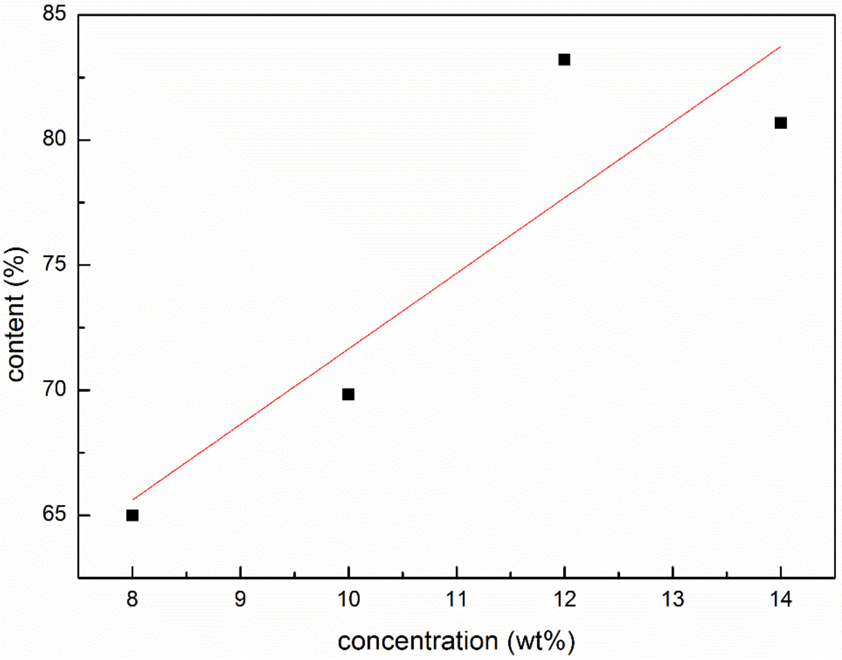

Fig. 28: Trending curve of β crystal phase ratios by changing the PVDF concentration.

However, in the lower concentration range, from 8 wt% to 12 wt%, in the semi-entangled regime, we would expect the higher molecular mobility to enhance the α-to-β transformation, with the electrostatic field having a positive effect on the change. These results don't allow us to conclude, definitely, if the α-to-β transformation happens in-flight or at the Taylor cone surface, unless there is a cooperative effect taking advantage from the chain entanglement, with the polarization of a small domain inducing the transformation on nearby domains, as it happens with magnetic properties of some materials. A possible way to test this hypothesis would be the calculation of the β ratio as function of acetone concentration. In this case, we would expect the higher evaporation rate to hinder the molecular mobility, thus reducing the β ratio, as well as the fiber stretching.

Interestingly, the results from FTIR spectra are consistent with the nanofiber morphology at different concentrations, with finer and more uniform nanofibers showing a higher β phase ratio. This behavior is reinforced with the analysis of other parameters' impact on the β phase ratio, described on the subsequent sections.

3.8 The effect of applied voltage on crystal phase structure

Common sense and theoretical review suggest that the higher the electrospinning voltage the better for converting the α to β phase structure. Fig. 29 (a) shows the FTIR-ATR absorption spectra of PVDF fibers obtained with different spinning voltages, with a spinning needle of 1.2 mm diameter and polymer concentration of 12 wt%. We did the same study with spinning needle diameter of 0.9 mm and solution concentration of 8 wt%. The FTIR-ATR spectra are shown in Fig. 29 (b).

The typical absorption peaks at 765 cm^{-1} and 841 cm^{-1} allow us to estimate the β content of the fibers, plotted in Fig. 30 for both experiments. The plot shows that β phase content increases linearly with the spinning voltage, nevertheless, the variation is significantly smaller than observed for the polymer concentration effect. Admitting the linear behavior to hold for higher voltages, the 100% β phase would only be achieved above 40 kV for (a) and 90 kV for (b). In a more conservative approach, assuming the linear behavior to be the early stage of an exponential approach to the total β phase, similar to a saturation behavior, the full β phase would only be reached well above 100 kV for (a) and above 300 kV. Either case, given the fact that the optimum spinning voltage was determined to be 24 kV, due to fiber morphology issues, it is not guaranteed that much higher spinning voltages can yield higher β contents and therefore we decided to keep the 24 kV as the optimum spinning voltage for next experiments.

As to the α-to-β transformation mechanism, the spinning voltage doesn’t clear the subject, but the larger needle and concentration yield fibers with higher β content, which is in line with previous observation that conditions leading to better fiber morphology also lead to higher β content, reinforcing the idea of a tradeoff between polymer chain mobility, electrostatic force and a possible cooperative effect, during flight between the needle and the collector.

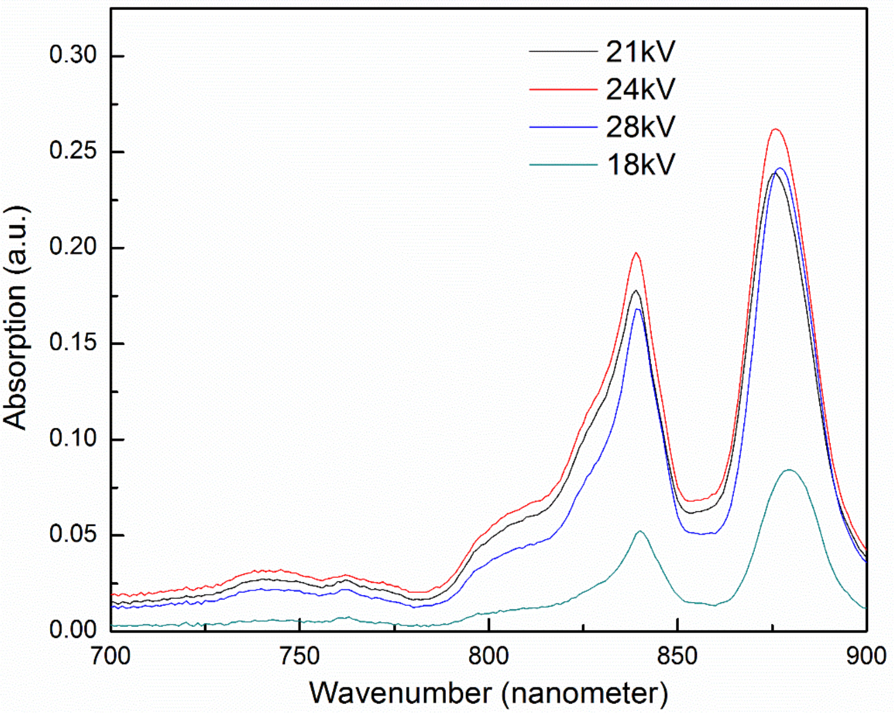

(a)

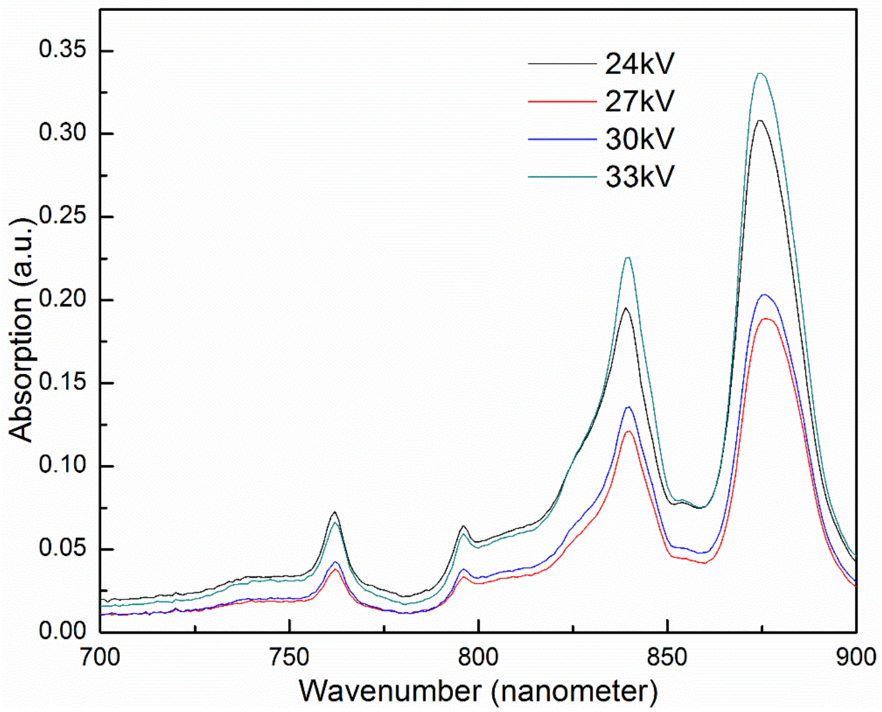

(b)

Fig. 29: FTIR-ATR spectrum of PVDF fibers obtained (a) at 18, 21, 24, 28 kV spinning voltage with 12 wt% concentration and 1.2 mm spinning needle; (b) at 24, 27, 30, 33 kV spinning voltage with 8 wt% concentration and 0.9 mm spinning needle; the other parameters were the same.

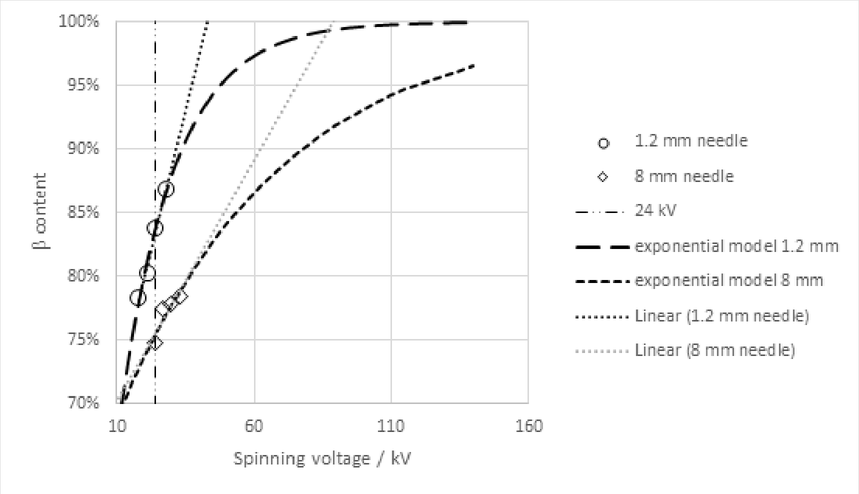

Fig. 30: Trending curve of β crystal phase ratios by changing voltages.

3.9 The effect of needle diameter on crystal phase structure

To isolate the combined effect of needle diameter and concentration observed in the previous section, and investigate the effect of needle diameter on crystal phase structure, we chose four different needle diameters, 0.5 mm, 0.8 mm, 0.9 mm and 1.2 mm, at constant concentration of 12 wt%, and applied voltage was 24 kV, spinning flow rate was 1.0 ml/h. The FTIR-ATR spectra are shown in Fig. 31. As we can see in Fig. 32, when the needle diameter increased, the β phase ratio increased as well. We had discussed before that when the needle diameter is small, the jet flow is also small, and so the initial electrostatic acceleration is higher, leading to shorter time-of-flight and poor fiber stretching. Again, the β phase ratio seems to correlate with the fiber stretching mechanism.

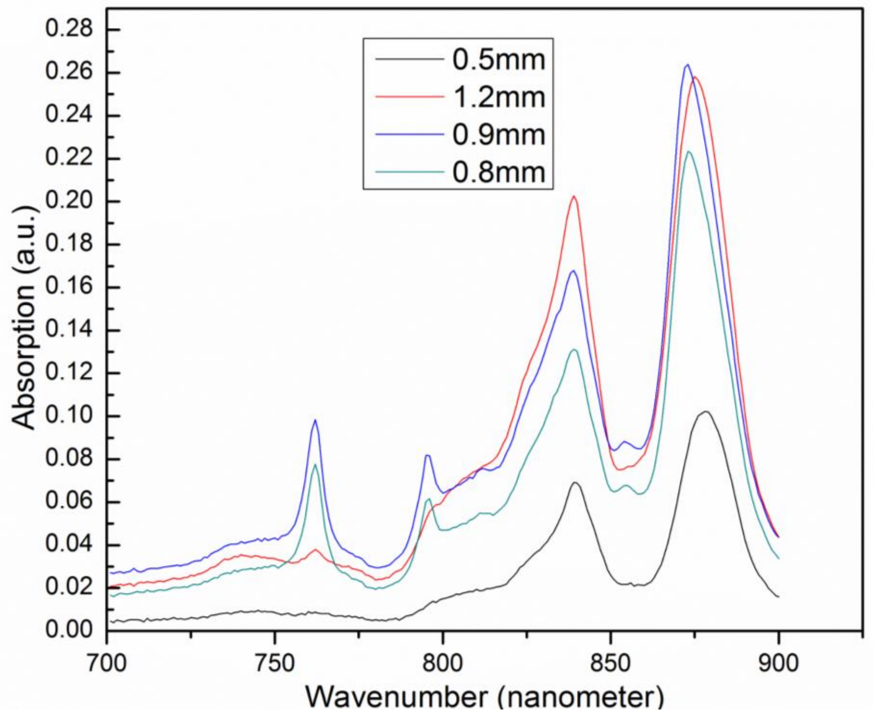

Fig. 31: FTIR-ATR spectrum of PVDF in different needle diameters.

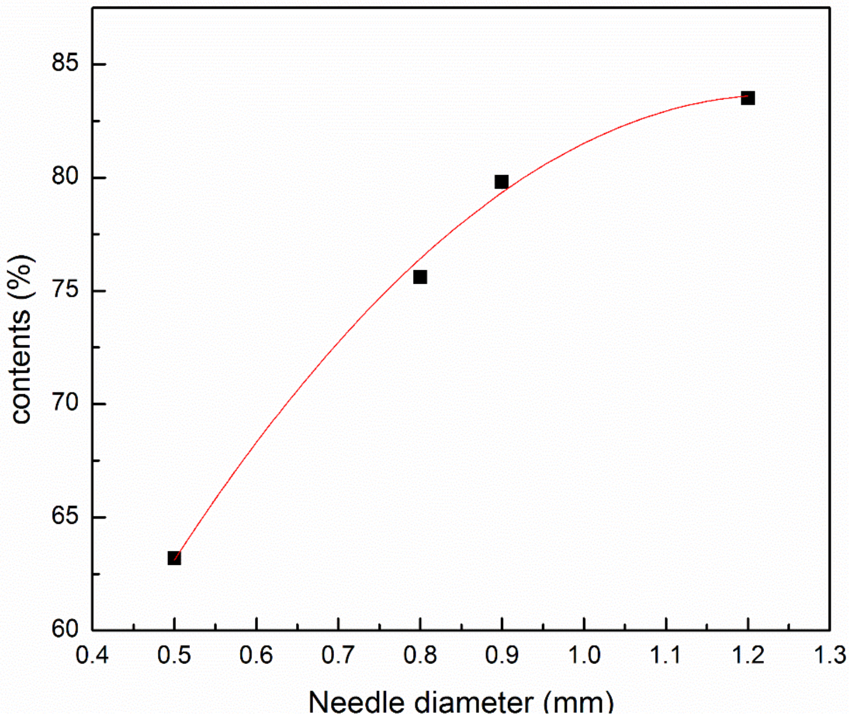

Fig. 32: Trending curve of β crystal phase ratios by changing needle diameters.

3.10 The effect of spinning speed on crystal phase structure

To test the effect of the spinning speed, on the β phase ratio of the PVDF fibers, we produced fibers with solution flow rates of 0.5, 1.0, 1.5 and 2.0 mL/h; the spinning voltage and needle diameter were set to 28 kV and 0.9 mm; the polymer concentration was 12 wt%. Fig. 33 and 34, shown the corresponding FTIR-ATR spectra and estimated β phase ratio for these four experiments. The trend is very clear and, again, it follows the fiber morphology effect as discussed before. Slower spinning speeds yield better shaped fibers with higher β phase ratio, although the difference between the β phase ratios at 0.5 and 1.0 is not significant. In this case, the explanation is not so clear, since the solution flow rate is more important for the mass transport of polymer to the tip of the needle. Higher flow means more polymer is available at the Taylor cone surface at therefore also there may be a change between full electrospinning and the onset of electrospray process, which may affect the jet profile and the stretching of the fibers.

The possible explain could be that the stretch force in the point of needle or interior of drops is not enough to make molecular chain aligned when spinning speed increased but electrical field force remained the same.

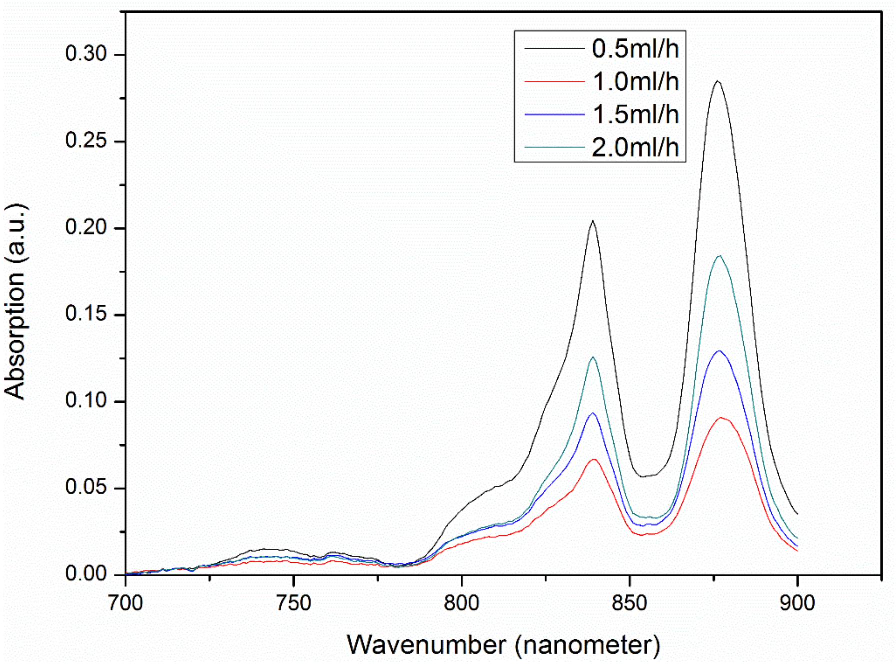

Fig. 33: FTIR-ATR spectrum of PVDF fibers produced with 0.5, 1.0, 1.5, and 2.0 mL/h flow rates.

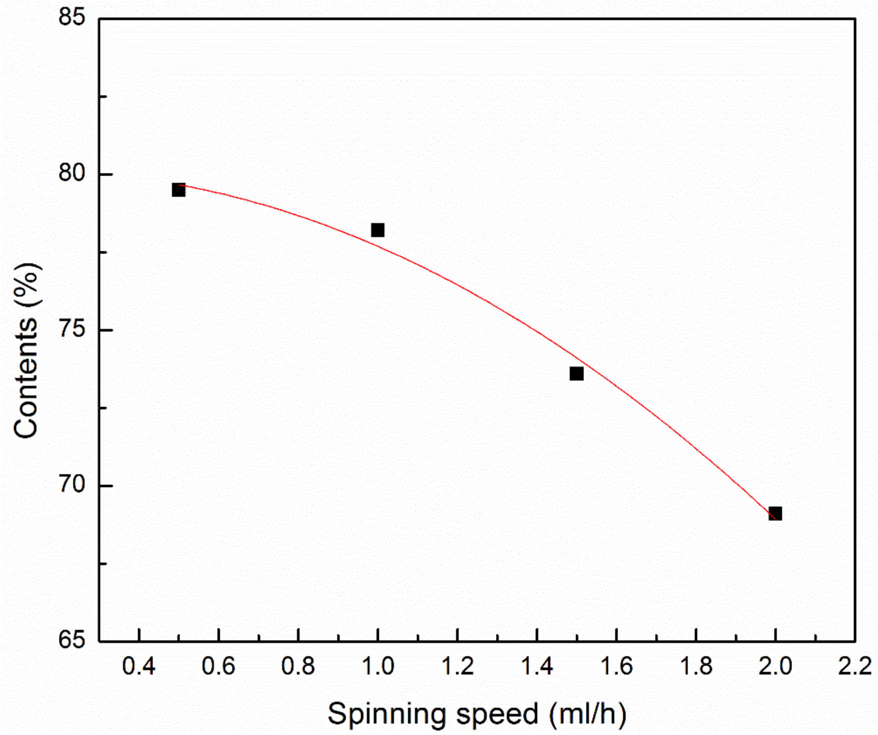

Fig. 34: Trending curve of β crystal phase ratios by changing spinning speed.

3.11 The effect of rotating speed on crystal phase structure

As demonstrated earlier, the collector's rotational motion influences positively the fiber morphology and alignment. Also, there seems to be a correlation between the fiber morphology and the β phase ratio on the fibers. The next obvious experiment is the investigation of the collector rotation on the β phase ratio. We produced PVDF fiber by changing rotating speed with the optimal experimental parameters obtained in previous sections, which were at 12 wt% concentration, 24 kV applied voltage, 1.2 mm spinning needle, and 1.0 spinning flow rate. From the FTIR-ATR spectrum in Fig. 35 we can see the characteristic peaks at 765 cm^{-1} are almost absent, comparing with the peaks at 841 cm^{-1}. This means there was much less α phase and the β phase ratio is enhanced by the rotating collector. It is clear from Fig. 36 that the β phase ratio is much higher than in previous experiments, increasing linearly with the rotation speed and reaching almost 90% at the top speed of 300 rpm. Once more, the fiber stretching and the β phase ratio seem to be linked. In this case, the additional pulling force resulting from the rotation, added to the electrostatic force, increases the fiber stretching and has a beneficial effect on the alignment of contiguous β phase domains along a preferred orientation. The cooperative effect previously discussed indeed seems to take advantage from the polymer chains stretching. It is important to notice that the baseline β phase ratio at 0 rpm is already well optimized and the rotating collector effect has a lower magnitude than the needle diameter. Nevertheless, it is an addition that, together with all the other optimized parameters, helps to bring the best β phase ratio up to 90%.

.

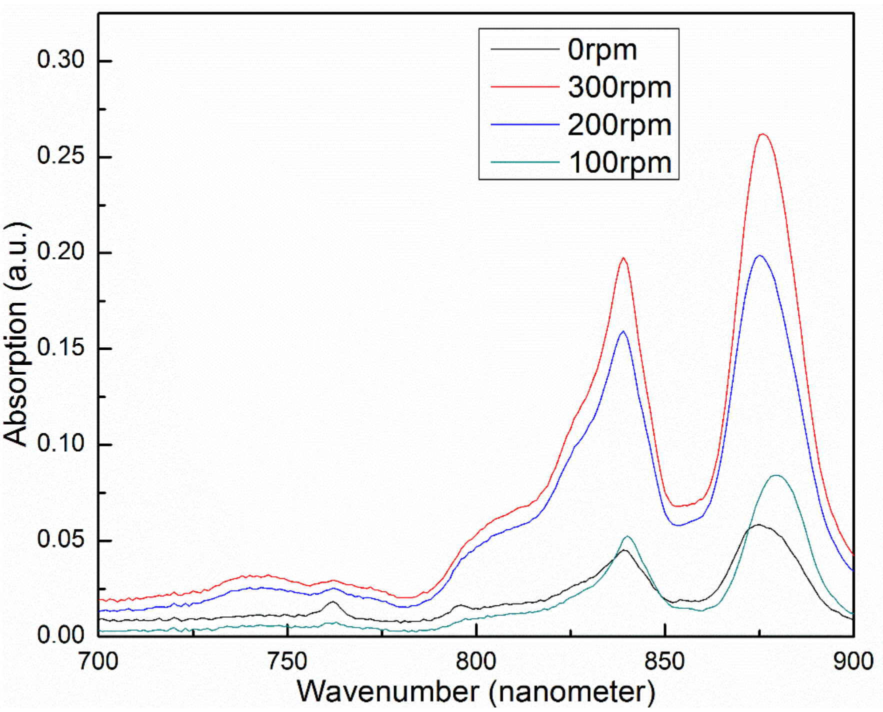

Fig. 35: FTIR-ATR spectrum of PVDF in different rotating speed.

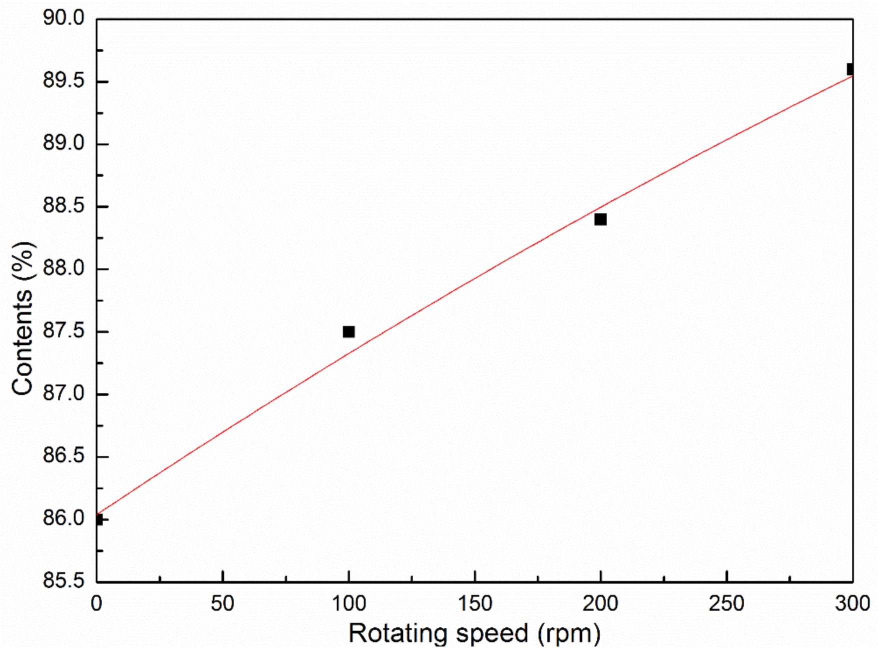

Fig. 36: Trending curve of β crystal phase ratios by changing rotating speed.

3.12 The effect of length on device impedance

The electrical impedance of a non conductive material, or dielectric, is a complex function of frequency, with a resistive (R) and reactive (X) components, or, alternativelly, an amplitude (Z) and a phase (θ).

$$\bar{Z} = R + j \cdot X = Z \cdot e^{j\theta} \qquad (3)$$

$$R = Z \cdot \cos\theta \qquad (13)$$

$$X = Z \cdot \sin\theta \qquad (14)$$

To enable its correct use for preparation of functional devices, it is important to know the electrical impedance of a material and its relation with the geometric properties of the device. In our case we wanted to relate the impedance of a fiber mesh to its geometric properties, length (L), width (W) and thickness (t), through its complex impeditivity $(\bar{\zeta})$, analogous to resistivity.

$$\bar{Z} = \bar{\zeta} \cdot \frac{L}{W \cdot t} \qquad (15)$$

By incorporating the thickness of the fiber mesh we get to a specific impeditivity $(\bar{\zeta}_S)$, which can be used to characterize our fibers' impedance as function of the frequency.

$$\bar{\zeta}_s = \frac{\bar{\zeta}}{t} \qquad (16)$$

Combining equations A, D and E allows us to represent the specific impeditivity as a complex function for the frequency, with an amplitude (ζ_s) related to the impedance, the length and width of the material, and the same phase as the impedance. The specific impeditivity is only dependent on the thickness and composition of the material.

$$\bar{\zeta}_s = \frac{Z \cdot W}{L} \cdot e^{j\theta} \qquad (17)$$

To study the electrical impedance of the PVDF fibers and the assembly of such fibers on electrodes, as discussed before, we prepared several devices with different distances between electrodes, of 1, 2, 4, 8 mm and constant width of 10 mm. The PVDF fiber mats used were prepared with the optimum conditions as discussed in previous sections.

Table. 8: Optimale conditions for fabricating PVDF mats.

Solvent	6/4 DMF/Acetone
Concentration	12 wt%
Applied Voltage	24 kV
Needle Diameter	1.2 mm
Spinning Flow Rate	1.0 ml/h
Rotating Speed	300 rpm

Fig. 37 and 38 show the impedance and the phase as a function of frequency. Fi. 39 shows the impedance values at the low and high frequency limits. We can see that the PVDF assembly exhibits the typical spectrum of a high pass filter made of a paralel RC circuit, as expected. The low frequency impedance is extremelly high, reaching the gigaOhm range, typical of an insulator, and is almost linearly dependent on the length of the fiber mat $(R^2 = 0.9741)$, as seen on Fig. 39. At this frequency range both the resistance and reactance are dominant over the device's impedance. The impedance decreases with increasing frequency, as the capacitive behaviour kicks in, offering a low reactance parallel path for electrical current. At the high frequency limit, the capacitive behavior of the PVDF fiber mat is neglible, the phase goes to zero, and the device impedance is just the contact resistance between fibers, electrodes and wires, plus the conductive ink resistance, with and average value of $7.23 \pm 0.05 \quad k\Omega$.

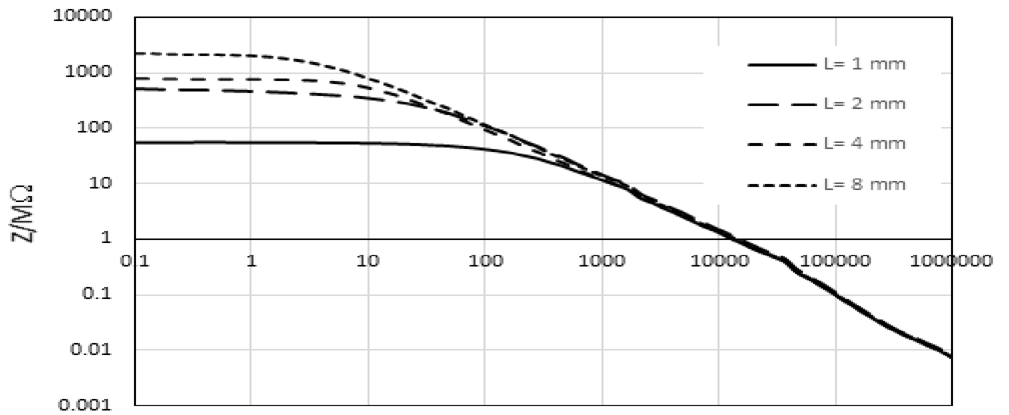

Fig. 37: Impedance amplitude of PVDF devices with constant width (10 mm) and variable length L.

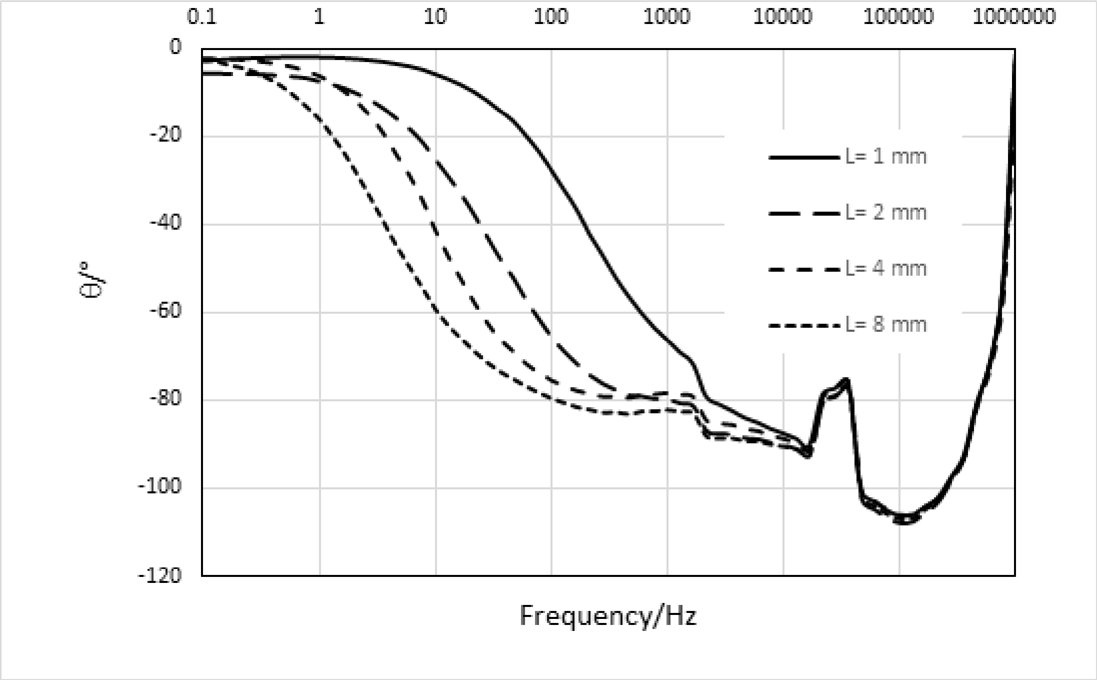

Fig. 38: Impedance phase shift of PVDF devices with constant width (10 mm) and variable length.

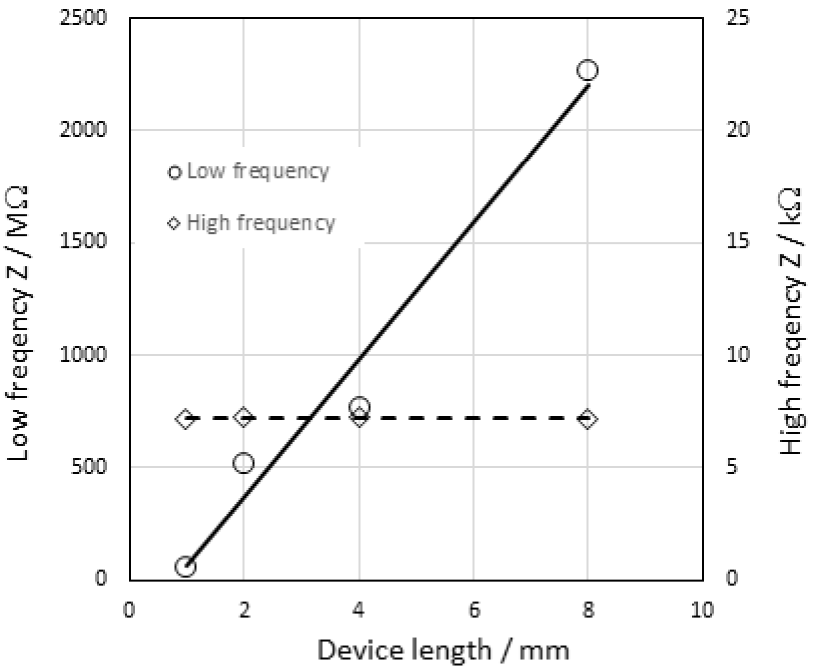

Fig. 39: Impedance values at the low and high frequency limits.

Typical piezoelectric devices are usually operated in one of five modes: radial, thickness, length extensional, thickness shear, length thickness. Due to the fiber mesh structure and the electrodes assembly, our devices don’t follow any of the typical piezoelectric modes of operation. For that reason, we didn’t expect to observe any resonance effect on the impedance measurements and indeed we don’t. Nevertheless, the impedance phase shift plotted on figure 40 presentes some interesting features to be analysed.

At first look, the phase shift seems typical of an RC device in series with a contact resistance, as pictures in Fig. 12: zero degrees phase at low frequency, due to the high resistive component of the polymer; decreasing towards -90° as the frequency dependent capacitive behavior becomes relevant; recovery to zero degrees at very high frequency, as the low contact resistance dominates. The capacitive behavior depends from the length and therefore there is a trend for the curves, with lower length, corresponding to lower capacity, shifting the curves towards higher frequency values.

The odd behaviour begins at low frequency, with a small and constant negative phase shift, which is frequency independent. This feature has been reported as usual for the low frequency phase shift of polymeric and biological materials[64] and requires a much more complex equivalent circuit to model it.

Secondly, in case the piezoelectric resonance condition is reached, the simple RC model from Fig. 12 is complemented with an inductor in series with the resistor R_2, to account for the electromechanical behaviour. The effect of the inductive component is to add a positive phase shift which changes the overall phase shift, increasing it to zero or even positive values at the resonance frequency. Our experimental phase shift follows the normal capacitive behaviour, reaching -90° around 1 kHz. But then, around 10 kHz, the phase shift goes below -90°, reaching almost -110° at 100 kHz. Also, between 16 kHz and 60 kHz, a sudden deviation of the phase from the monotonic trend can be observed. This deviation shows up in all our impedance measurements and is independent of the device's geometric properties. There are two possible explanations for the deviation. First, it could an artifact from experimental measurement, due to some equipment malfunction. But it could also mean a more complex electrical behaviour, due to the onset of the resonance conditions. The lower than -90° phase shift, which appears from 10 kHz to 400 kHz, independently from the device length, is equivalent to an apparent negative resistance. Since resistance is the derivative of the voltage with respect to the current, a negative resistance means that electrical current is flowing in a direction opposite to the expected, which may be a consequence of the piezolectric effect. Apparent negative resistances have been observed in carbon fiber composites and other exotic materials[65] , but not in PVDF electrospun fibers, and therefore this behaviour in deserves further investigation, to confirm or dismiss the observed deviation.

Fig. 40 shows the calculated specific impeditivity ζ_s as function of the frequency. From equation E, we expected the specific impeditivity to be affected by the thickness of the fiber mesh the same for all different lengths tested. Fig. 40, together with the not so good correlation $(R^2 = 0.9741)$ of the low frequency impedance, shows that there must be some non-uniformity on the thickness of the electrospun fiber meshes, which, for highly reproducible results, will require more effort into controlling the deposition process.

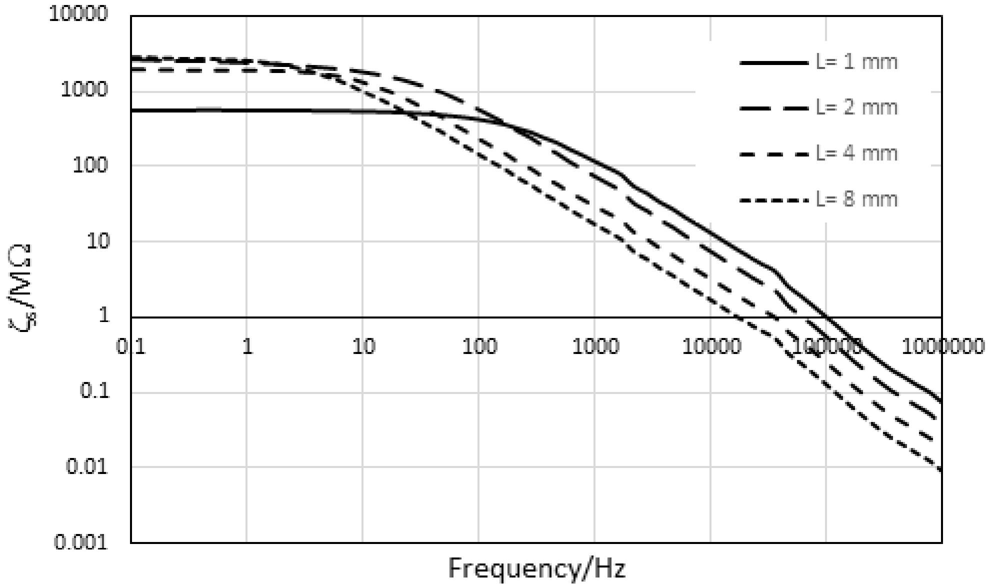

Fig. 40: Specific impeditivity of the PVDF devices with constant width (10 mm) and variable length.

3.13 The effect of width on device impedance

Following the results from section 3.14, we prepared sereval assemblies with different widths (10, 5, 2 and 1 mm) and constant length of 1 mm. The electrical impedance was measured and plotted against frequency, in Fig. 41 and 42. Fig. 41 shows the expected behaviour of the impedance as function of the width. Similarly to the previous experiments, the low and high frequency limits were plotted against the reciprocal of the width, in Fig. 43. The low frequency impedance follows a linear trend $(R^2 = 0.9939)$, as expected from equation D, and the high frequency impedance is constant and consistent with previous data. The device with 10 mm width exhibited outstandingly low impedance.

The impedance phase shift in Fig. 42 is very similar to Fig. 38, including the small frequency independent negative value at low frequency, the normal capacitive behaviour, the strange deviation from monotonic and the lower than -90° at high frequency.

The specific impeditivity ζ_s, plotted in firgure 46 as function of frequency and width, shows a similar behaviour to the variable length study. The device with the largest width, 10 mm, exhibits the lowest impeditivity, perhaps due to higher thickness of the fiber mat.

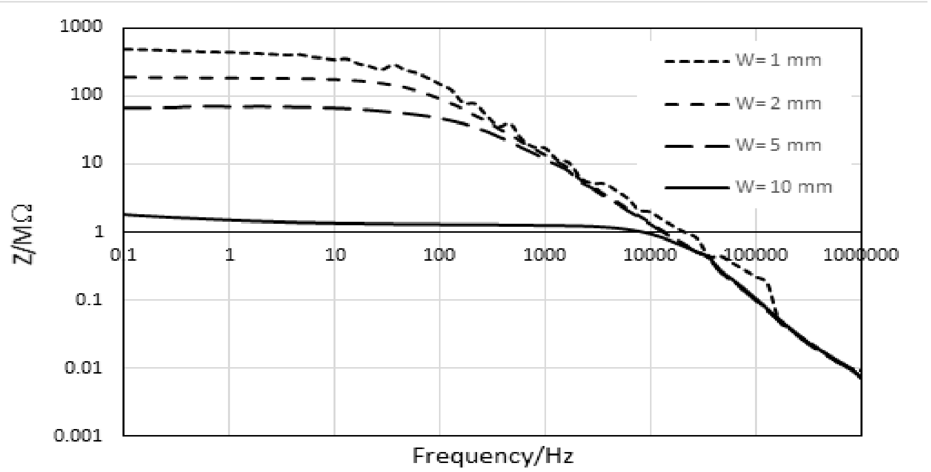

Fig. 41: Impedance amplitude of PVDF devices with constant length (1 mm) and variable width W.

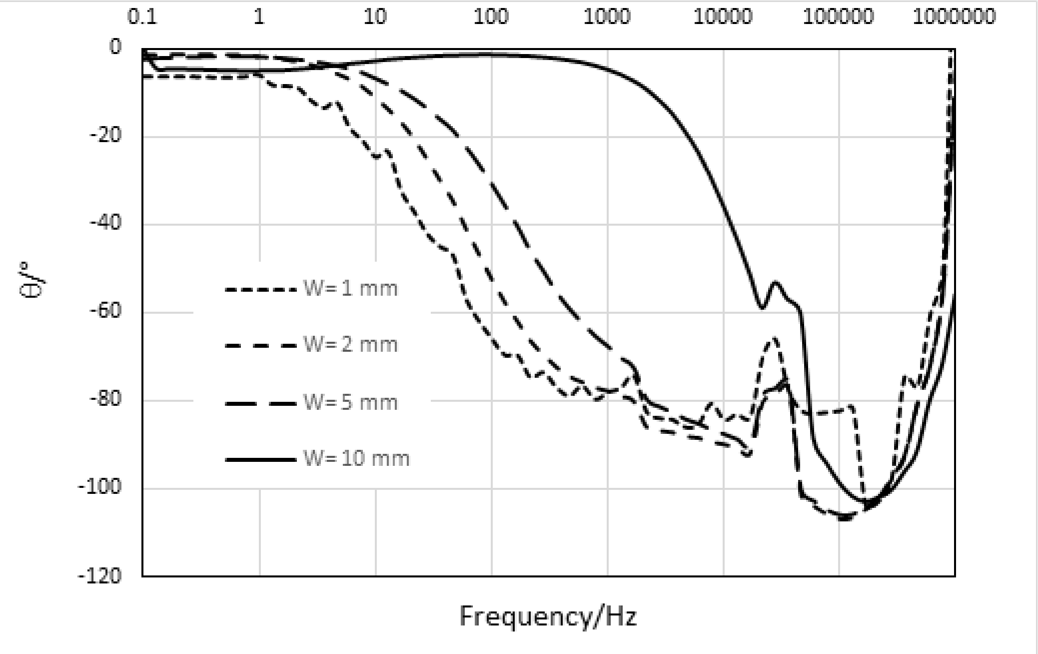

Fig. 42: Impedance phase shift of PVDF devices with constant length (1 mm) and variable width.

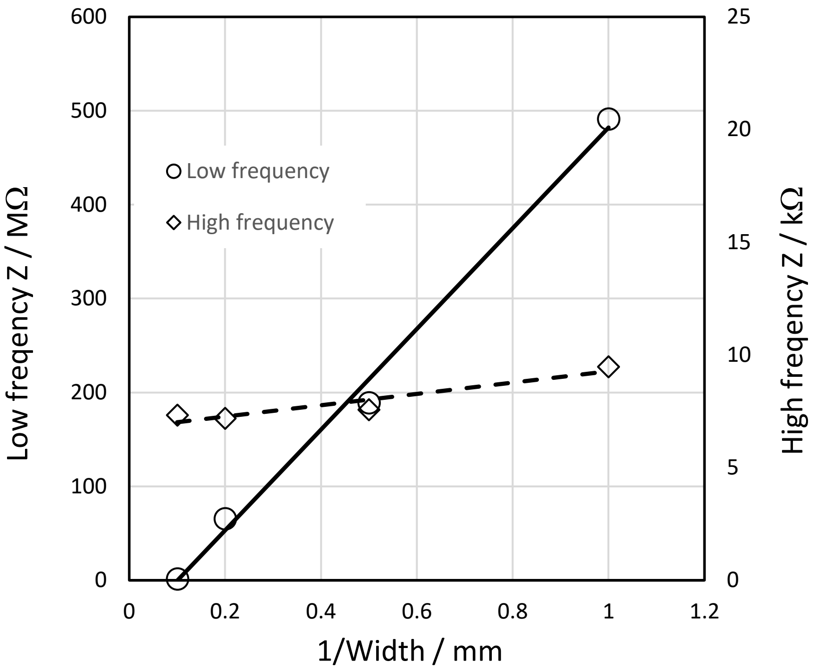

Fig. 43: Impedance values at the low and high frequency limits.

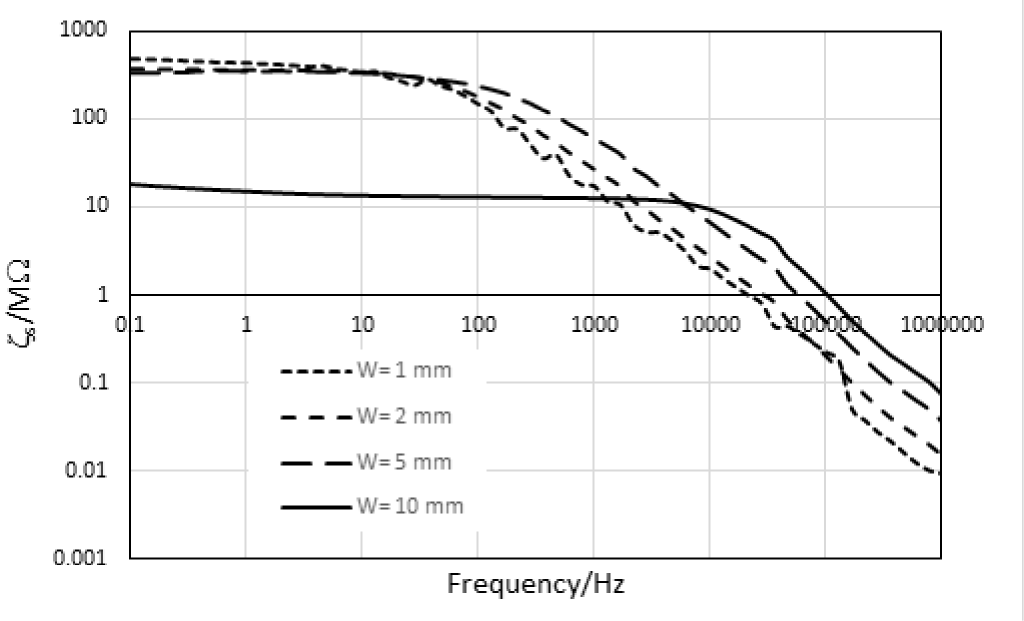

Fig. 44: Specific impeditivity of the PVDF devices with constant length (1 mm) and variable width.

Both the length and the width variation studies included data on two devices with similar characteristics: length $L = 1\ mm$; width $W = 10\ mm$. Although the geometric properties and composition are the same and the two devices are the best performant on each series, in fact they ehxibit much different inpedance values, as can be seen from Fig. 45 and 46. The device from the length study has a low frequency impedance, corresponding to the dielectric resistance of the fiber mat, which is 30 to 40 times higher than the other, from the width study. At the high frequency limit, which corresponds to the contact resistance value, the ratio of impedances has a value of 1. These results confirm the strong depence of the fibers' impedance with the fiber mat thickness. Thicker fiber mats have higher dielectric resistance and also higher capacity. The higher capacity explains the deviation of the *width study* device's phase shift to higher frequencies. Fig. 47 shows the resistive and reactive (capacitive) components of both devices, where the scale factor is very clear. This plot also highlights the small negative resistance window that results from the excessivelly negative phase shift at high frequencies.

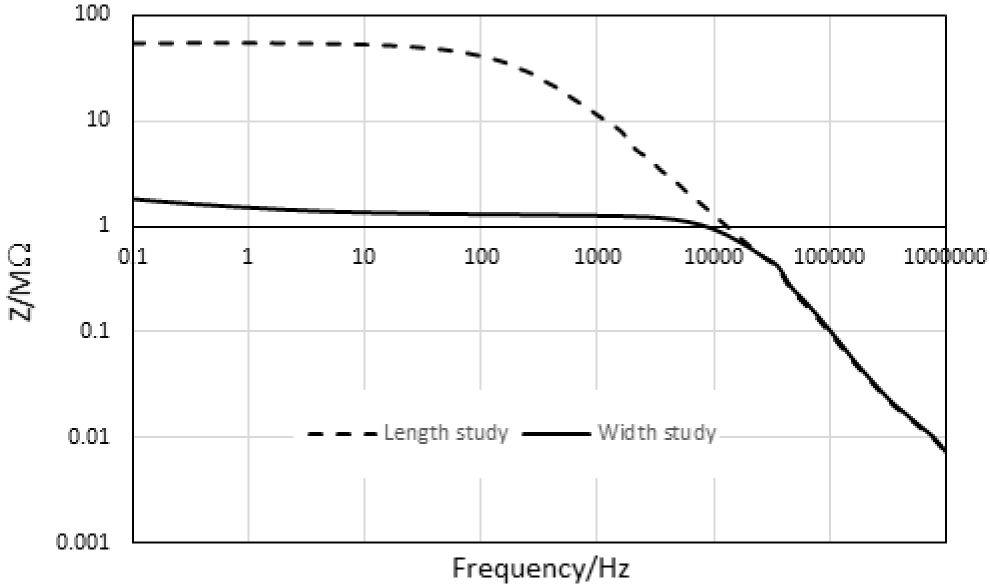

Fig. 45: Impedance amplitude of two PVDF devices with the same length and width: $L = 1\ mm, W = 10\ mm$.

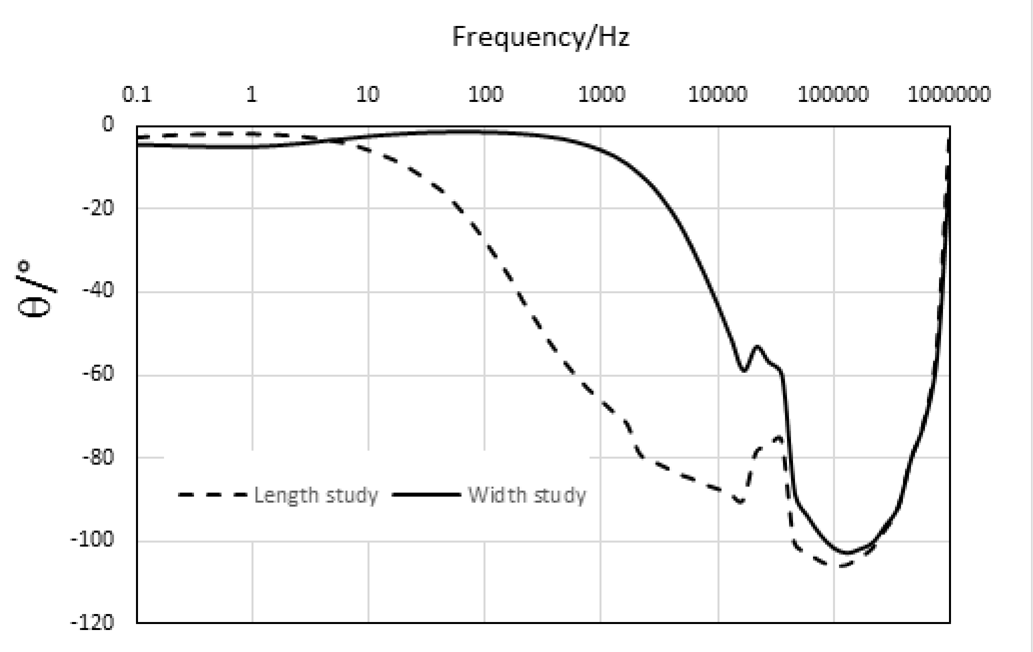

Fig. 46: Impedance phase shift of two PVDF devices with the same length and width: $L = 1\ \ mm, W = 10\ \ mm$.

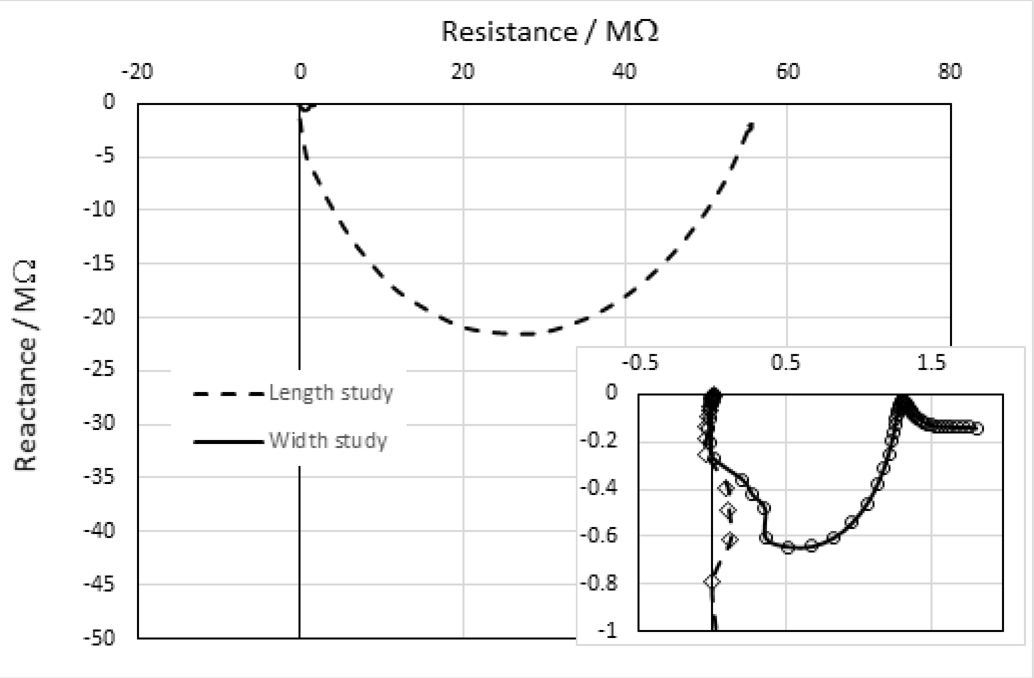

Fig. 47: *Nyquist* plot of the resistive and reactive components of the two best PVDF devices with the same length and width: $L = 1\ \ mm, W = 10\ \ mm$. The inset shows the small area around the origin.

3.14 Fitting between experimental data and electrical model

The best data set from the length and width studies, with the lower impedance, was fitted to the simple equivalent circuit of Fig. 12, with R_1 representing the contact resistance, R_2 and C representing the dielectric resistance and capacitance of the fiber mat. The result is plotted in Fig. 48 through 50. Our best effort with the simple RC model wasn't satisfactory. It turns out that the RC model cannot account for the overall behaviour of our system. The contact resistance has an almost irrelevant contribution to the model and the constant parameters R_2 and C are not enough to describe the experimental data. The best fit of the impedance occurs only in a limited range of frequencies, between 1 kHz and 100 kHz. The RC model cannot fit the low frequency behaviour, for which the system behaves as a variable capacitance that compensates the frequency increase to keep a constant phase shift. The apparent negative resistance at high frequencies cannot be fitted also. We used the reactance values to calculate the apparent capacitance of the device, plotted in Fig. 51. The capacitance between 1 kH and 100 kHz is within 10 pF to 1 nF, which is a reasonable. In the low frequency region the device's capacitance shows a unusual broad range from 10 μF to 1 nF, which cover several orders of magnitude. Only the impedance amplitude could be modelled; any attemp to fit the phase shift failed completely. Other studies implement a much more complex model, including a variable capacitor to account for the constant phase shift at low frequency. We didn't succeed in fitting our data with this model and therefore future work is required for an adequate description of the PVDF fibers behaviour. The high frequency apparent negative resistance also deserves further study, to clarify if the data is valid and understand its origin. It is possible that the piezoelectric effect may be causing the negative resistance and the PVDF fiber might be acting as an acoustic sensor in the ultrasound range.

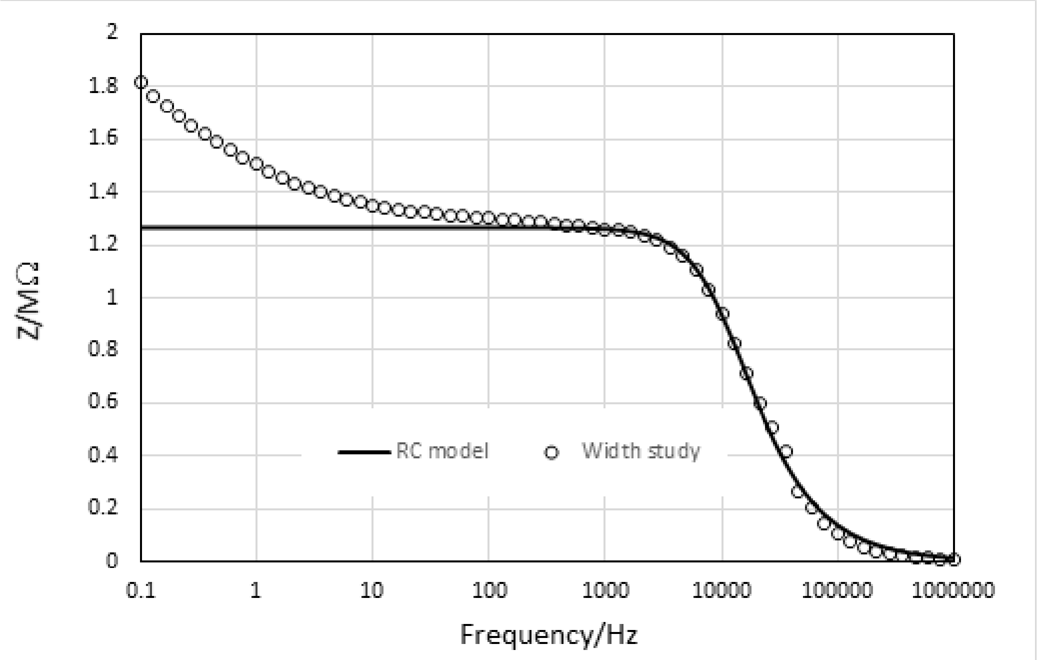

Fig. 48: Plot of experimental impedance versus the simple RC model.

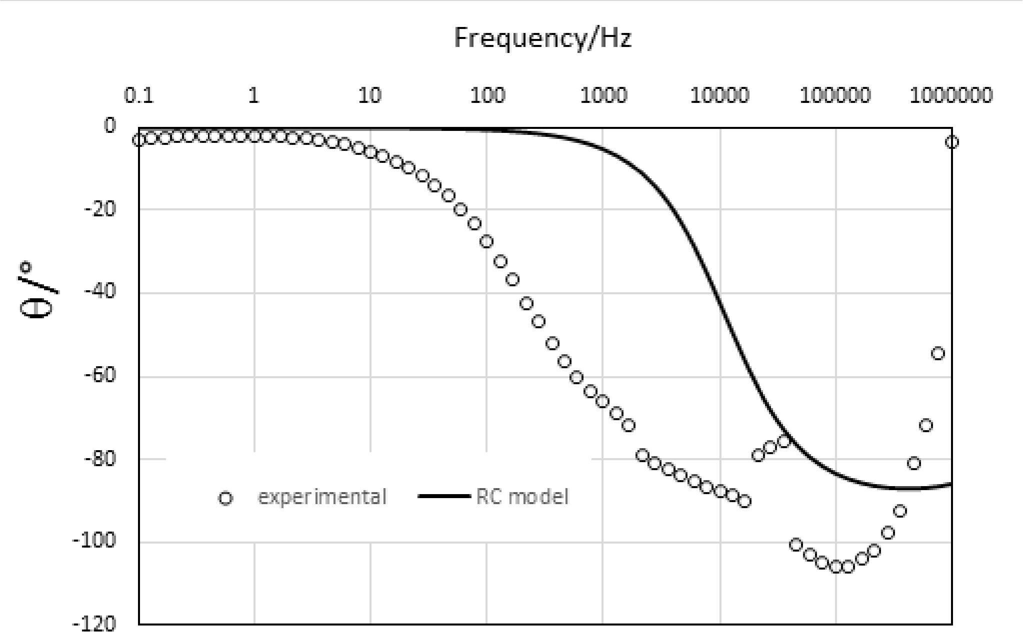

Fig. 49: Fitting trending curve of phase against frequency, blue curve represents experimental data, red curve represents modeling data.

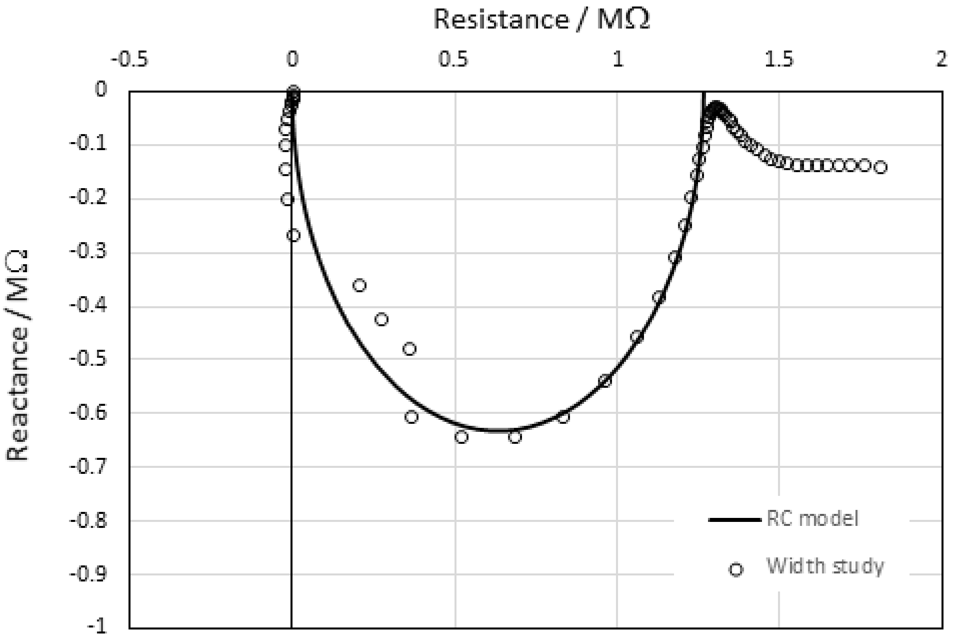

Fig. 50: Nyquist plot of the resistive and reactive components of the device’s impedance and RC model.

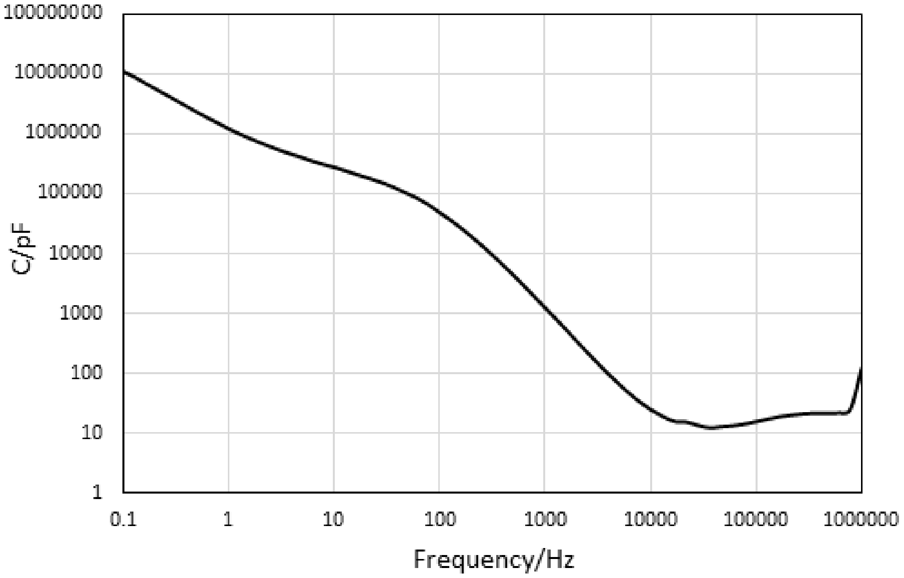

Fig. 51: Apparent capacity.

We fitted all the devices from the length study with the RC model, the results are shown in table. 9. We notice that the fixed capacitance is always in the tens of pF and the dielectric resistance increases with the length, as noted before. The contact resistance

R_1 is always low and its contribution for the model is insignificant.

Table. 9: Elements values of equivalent circuit with different effective length.

W/mm	L/mm	R_1/kΩ	R_2/MΩ	C/pF
10	1	1	1.29	11.5
10	2	1	66	33.2
10	4	1	150	19.4
10	8	1	5000	10.9

We also fitted the width study data woth the same RC model and got similar results as shown in table : the 1 kOhm contact resistance, the tens of pF capacitance and the dielectric resistance inverselly proportional to the width.

Table. 10: Elements values of equivalent circuit with different effective width.

W/mm	L/mm	R_1/kΩ	R_2/MΩ	C/pF
2	1	1	330	15.0
5	1	1	180	15.9
10	1	1	1.26	11.5

3.15 The effect of β phase ratio on the impedance

We have previouslly discussed the effet of the spinning speed on the β phase ratio of the PVDF fibers, values decreased with an increase in spinning speed, and the β ratio was highest, close to 80%, at a spinning speed of 0.5mL/h.

Fig. 47 shows that the low frequency impedance also changed with the spinning speed, the β phase ratio and impedance showed a inverse relation to the spinning speed. These results suggest that uniform and fine PVDF nanofibers with higher β phase ratio should have lower impedance, which could present a reason for the observed variability of the capacity at low frequenecy

In this study, it was interesting to find that more uniform and finer PVDF fibers showed higher β phase ratio which leading to lower electrical impedance regardless the changes of spinning concerntration and electrospinning parameters. The impedance changes followed the inversive trend to the change of β phase ratio whatever the change was caused by polymer solution concerntrations or operating parameters. Fine and uniform nanofibers with small diameters and high β crystal phase ratio facilitate to electric-to-mechanical energy conversion. Well aligned fiber meshes in one direction also enhance the higher β phase ratio. These understanding could be helpful to develop piezoelectric devices or electroacuators for various applications in tissue engeneering and electric field..

3.16 MTT assay

The cytocompatibility of all samples was evaluated by MTT cell viability assay (Fig. 52). MTT assay data show that the viability of NIH/3T3 cells incubated with the PBS and different samples is around 100%. The bar errors are 6.54%, 4.24%, 5.42% and 1.10% respectively. Number 1 means PBS cultured cells and Number 2 represents PVDF fiber mash culturing cells. Number 3 and 4 represent PVDF/PLGA and PLGA fiber mesh samples respectively. For number 3 and 4, the cell viability just slightly decreases to 99.59% and 98.97% accordingly. This suggests that PVDF has no effect on cytocompatibility of PLGA, PVDF fiber mesh even has better cytocompatibility than which of PLGA fiber mesh.

The results in Fig. 52 shown that all the samples caused no obvious loss of cell viability in NIH/3T3 cells comparing with the cells treated by PBS buffer. It was clear that PVDF fiber meshes were non-toxic.

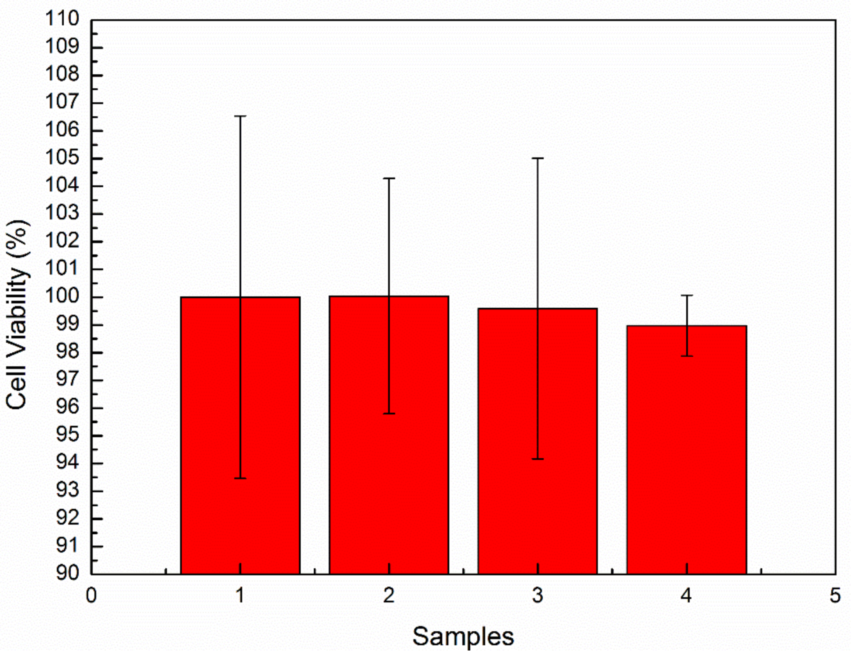

Fig. 52: Results of cell cytocompatibility.

CHAPTER 4 – MOLECULAR MODELLING

The quantum mechanics study of single, short, polymer chains with 8 and 16 monomer units, in both perfect crystalline α and β conformations, allowed us to analyze the atomic point charges, energy, torsional angles and dipoles of single polymer chains. But the semiempirical or the ab initio geometry optimizations yield perfect structures with no link to the dynamic mechanisms behind the phase change. The realization of molecular dynamic (MD) studies with quantum mechanics for longer polymer chains would be unfeasible with the available computation resources. Therefore, we turned to molecular mechanics and the AMBER99 force field, in order to study the effect of an externally applied electric field on the conformation of PVDF polymer chains.

For the MD studies we built a single PVDF polymer chain with 64 monomer units and perfect α conformation on all monomer units. Fixed atomic point charges were allocated with the *Gasteiger-Marsili*'s *partial equalization of orbital electronegativities* algorithm. The polymer chain was duplicate and the two resulting chains were subject to a MD calculation at a constant temperature of 500 K for 500 ps until equilibrium was reached. Then followed a similar process at 100 K for the same period. All the torsional angles (γ) on both chains, in a total of 126, were recorded at each MD data step. At the end of the equilibration runs we got a *ball* shaped particle with an approximate diameter of 3 nm, and both chains were entangled. To account for the total α or β conformations we compared every torsional angle γ with reference values of 60° for α and 180° for β, as summarized in the following rule.

$$Torsion\ \ is\ \begin{cases} \beta \quad \Leftarrow \quad |\gamma - 180°| \geq |\gamma - 60°| \\ \\ \propto \quad \Leftarrow \quad |\gamma - 180°| < |\gamma - 60°| \end{cases} \tag{18}$$

After the equilibration runs, the β type units accounted to 18.25% of all the 126 torsional angles. The choice of this *hard* rule was dictated by simplicity. A *softer* rule could be used, through a statistical analysis of all the torsional angles at each data step, but it is likely it would yield very similar results.

To simulate the impact of the externally applied electric field, used on the electrospinning process, the equilibrated system was subject to a subsequent MD runs at constant 100 K temperature, with a duration of 100 ps and 1 fs data steps. All the torsional angles were recorded at every 100 data steps. After the MD run, the recorded torsional angles were analyzed and the β% was calculated at each data step.

For this MD, as shown in Fig. 53, a uniform electric field with fixed intensity (in arbitrary units) was simulated along the x axis of the system. The conversion factor from the arbitrary units to real S.I. units was calibrated with a separate series of MD calculations with a fluoride ion, to determine the acceleration produced under different electric fields. The conversion factor was found to be $12628.18159 \pm 0.00002 \ \ \mathrm{MVolt} \cdot \mathrm{m}^{-1}/a.u.$

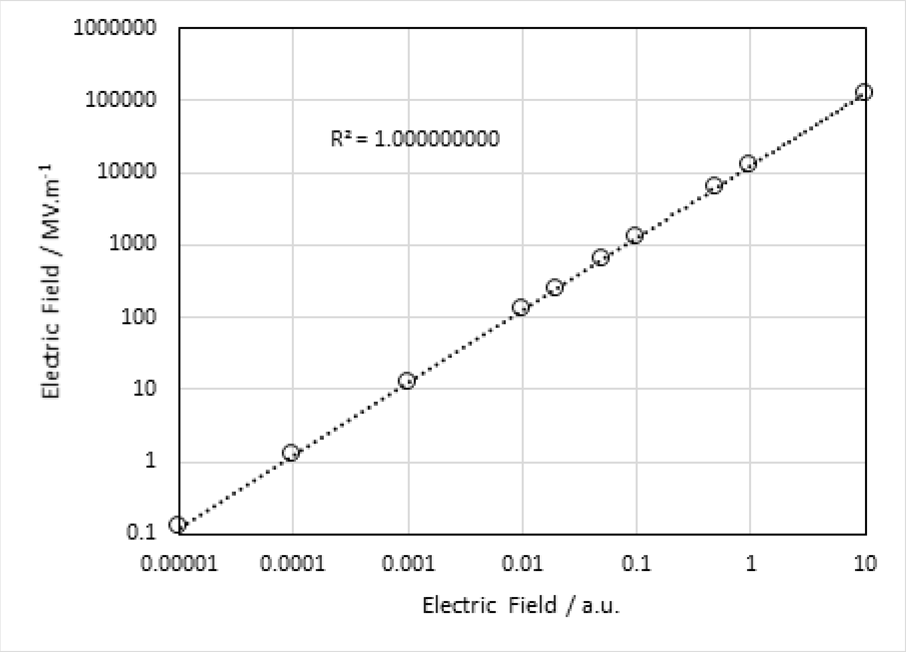

Fig. 53: Calibration of the uniform electric field.

A total of 25 MD runs under a uniform electric were performed, as shown in Fig. 54 and table. 11, covering a wide range of electric field values.

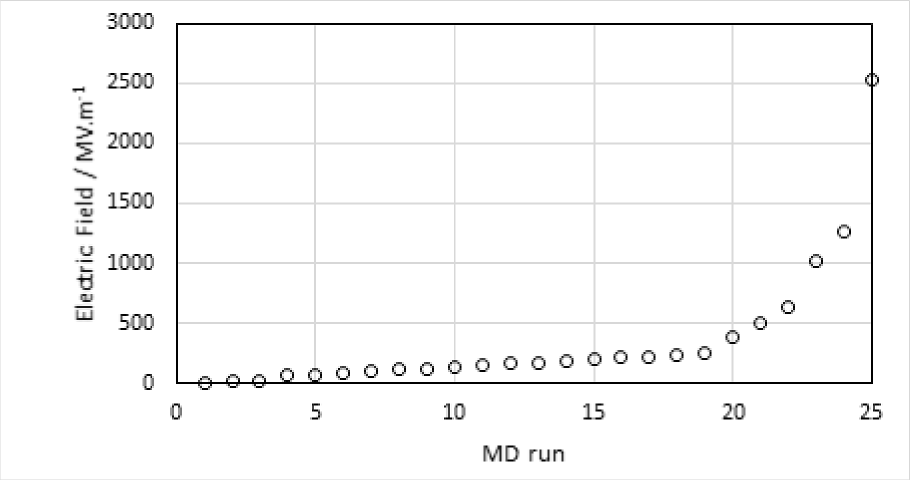

Fig. 54: The total runs under a uniform electric.

Table. 11: The Ex (a.u.) and Ex/MV.m^{-1} values in 25 runs.

MD run	Ex (a.u.)	Ex/MV.m^{-1}	MD run	Ex (a.u.)	Ex/MV.m^{-1}
1	0	0	14	0.015	189.4
2	0.001	12.6	15	0.016	202.1
3	0.002	25.3	16	0.017	214.7
4	0.005	63.1	17	0.018	227.3
5	0.006	75.8	18	0.019	239.9
6	0.007	88.4	19	0.02	252.6
7	0.008	101.0	20	0.03	378.8
8	0.009	113.7	21	0.04	505.1
9	0.01	126.3	22	0.05	631.4
10	0.011	138.9	23	0.08	1010.3
11	0.012	151.5	24	0.1	1262.8
12	0.013	164.2	25	0.2	2525.6
13	0.014	176.8			

The results of the full MD study are plotted in Fig. 55 and 56.

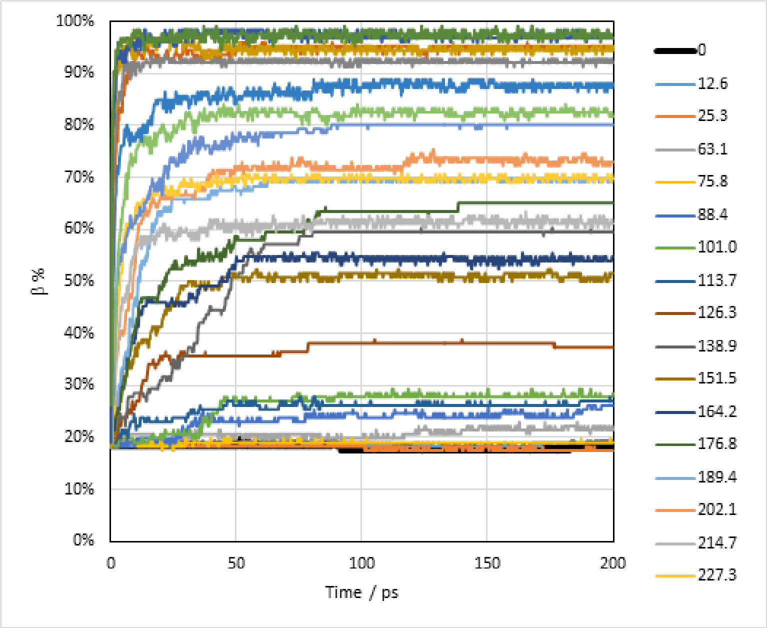

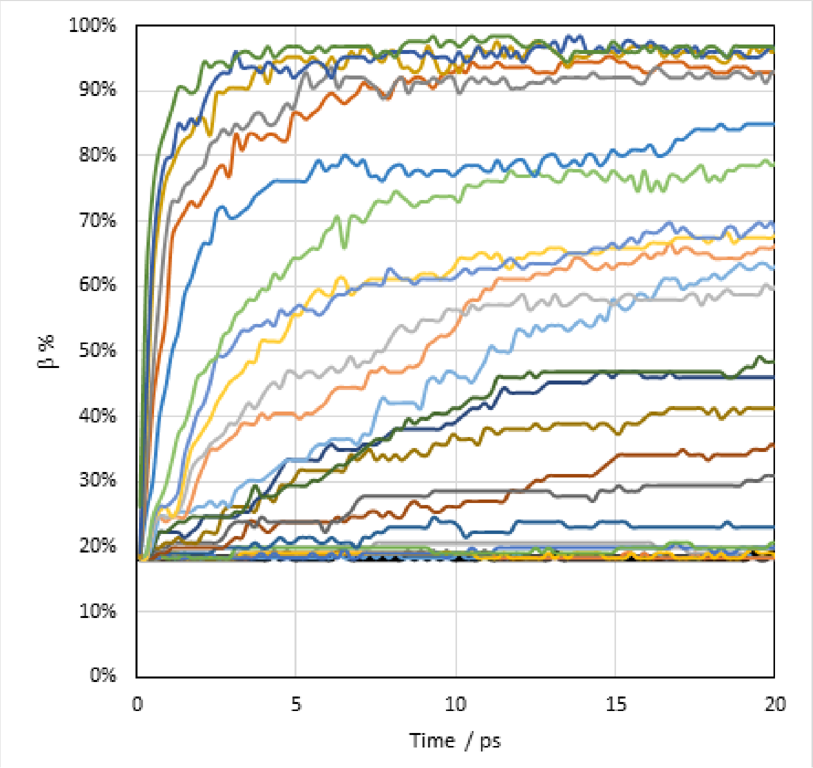

Fig. 55: β% calculated from the molecular dynamic simulations at different electric field values (MV.m^{-1}). Top, all data set. Bottom, detail below 20 ps.

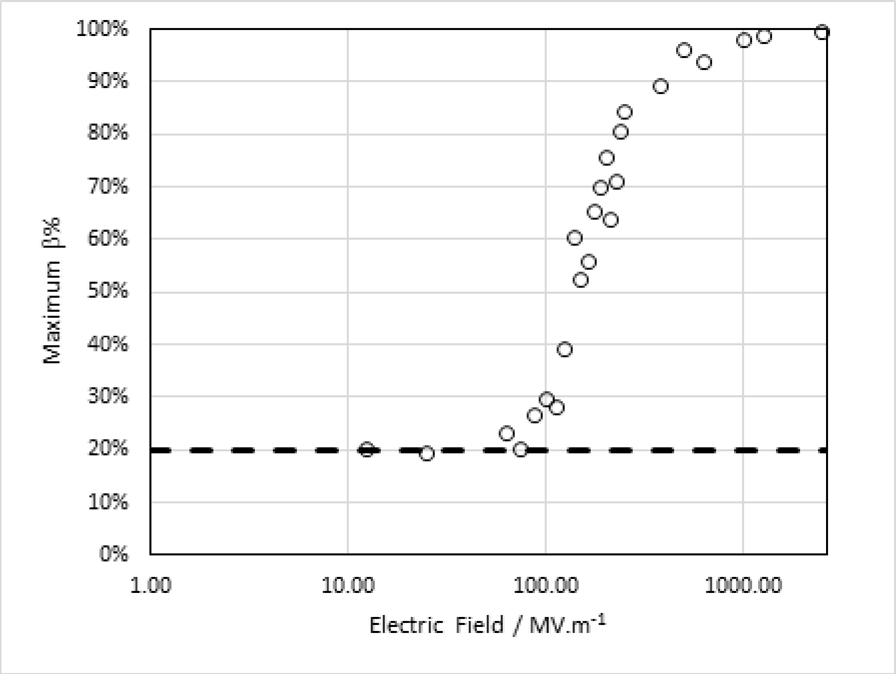

Fig. 56: Plot of the maximum β% of at the end of each MD run.

We can see that the percentage of torsional angles, or monomer units, with the b configuration starts at the equilibration state, around 20%, and increases with the electric field. There seems to be a threshold, or critical value, around 100 MV.m^{-1}, above which the conversion from α to β increases dramatically, and the β% seems to saturate to 100% at larger electric field intensities.

Our simulation data agrees with the experimental observation that higher electrospinning voltages generate higher percentage of β PVDF in the fibers. Typical voltages between 10 kV to 30 kV, with distances of 10 to 20 cm, generate electric fields in the range of 0.05 to 0.3 MV.m^{-1}, which is significantly lower than field values used in our study. But the time-of-flight of a polymer jet is several orders of magnitude higher than our MD duration time. It is admissible that for simulation runs closer to the real time-of-flight, even low intensity simulated electric fields can approach the experimental outcome.

Since we used just a small PVDF sample, two small chains, our simulation results don't allow us to establish if the α to β conversion happens in flight, or at the boundary between the liquid solution and surrounding air.

For each run, the β% values fit a simple exponential equation with three parameters (Fig. 57), where *A* is the saturation value, *B* is the starting value and *C* is a time constant.

$$\beta\% = A + (A - B)e^{-t/c} \qquad (19)$$

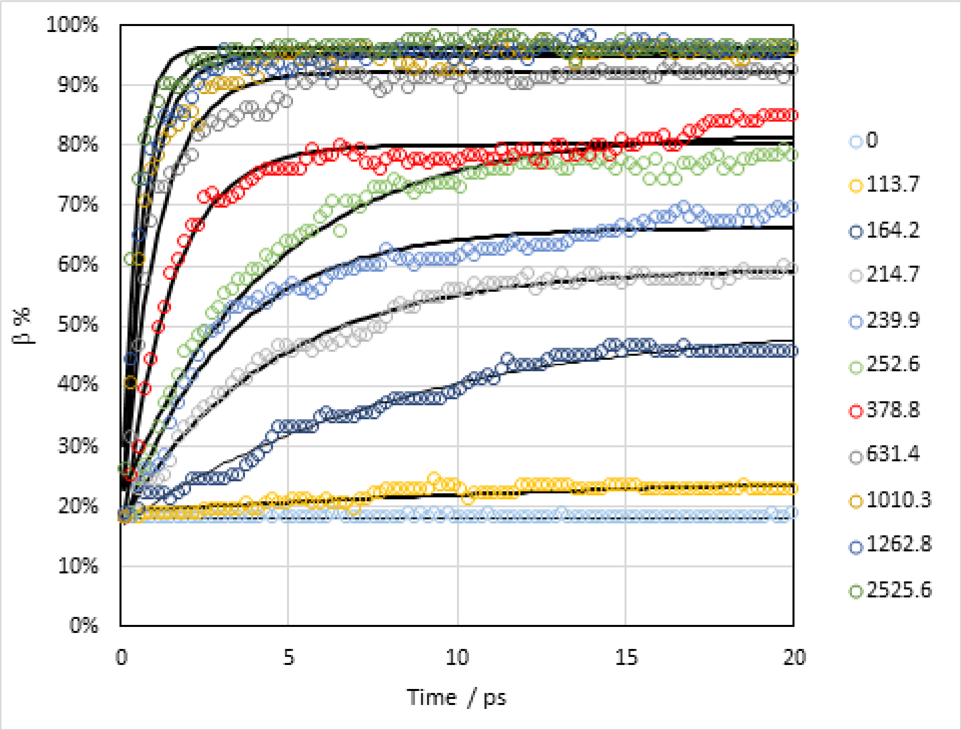

Fig. 57: Plot of selected data fitted with equation 19.

The following images in Fig. 58 show the final MD run appearance of the PVDF sample at selected electric field intensities (0, 113.65, 214.68, 378.85, 1010.25, 1262.82, 2525.64 MV.m^{-1}). Some snapshots are seen from the *z* axis (*xy* projection) and some from both the *z* axis and *x* axis (*yz* projection) which is the electric field direction. It is clear that higher field intensity, results on more β domains. Also, other than just converting PVDF from α to β, higher fields stretch the polymer chains, from the globular shape to a straight one. We had concluded from our experimental data, that mechanical deformation from the spinning process is likely to help on the conversion and both, electric field and applied force, act with a synergic effect.

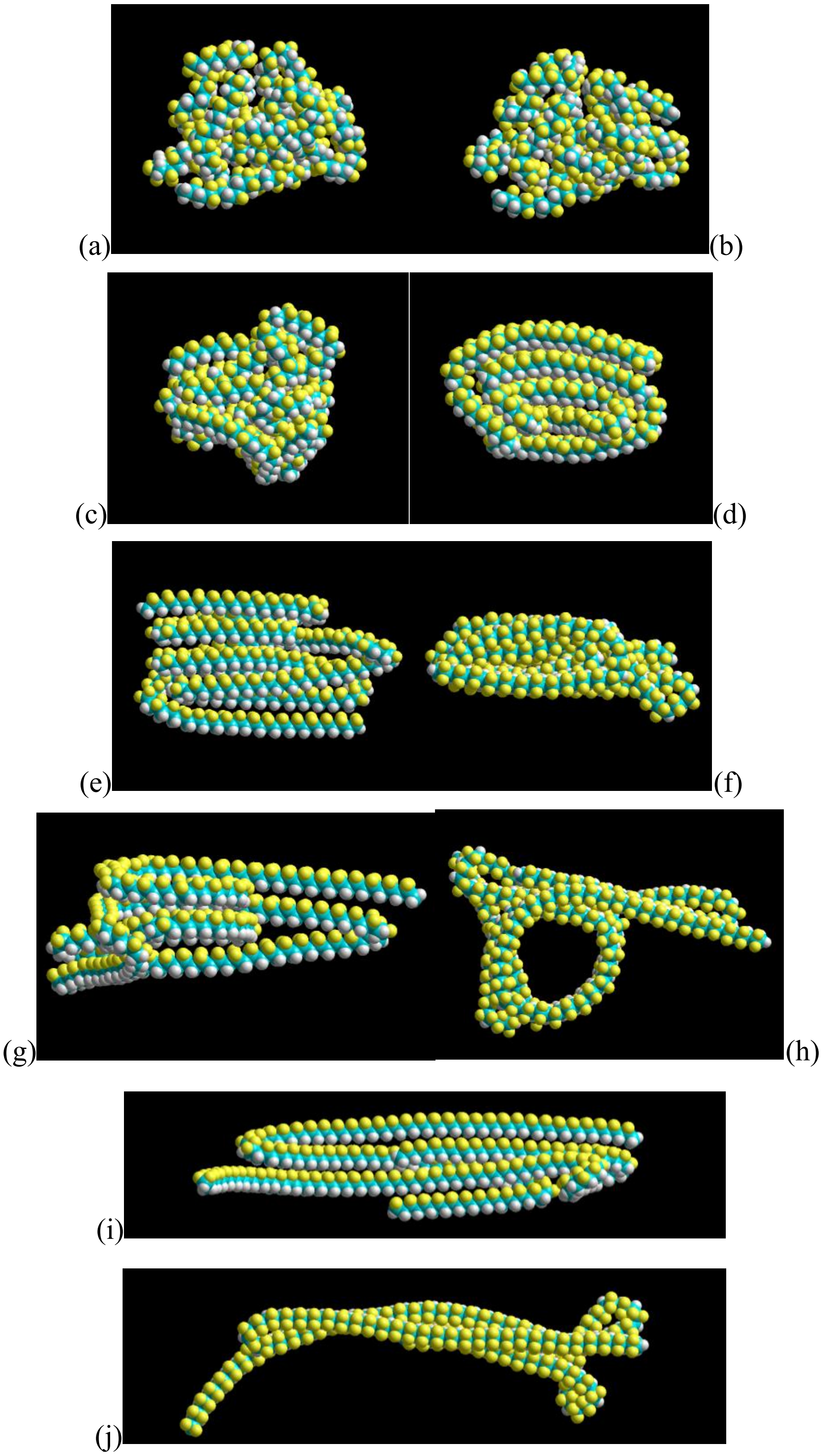

Fig. 58: Final MD run snapshots (*xy* projection) of the two PVDF polymer chains under selected electric field intensities (MV.m^{-1}): (a) 0; (b) 113.65; (c) 214.68; (d) 378.85; (e) and (f) 1010.25, *xy* and *yz* projections; (g) and (h) 1262.82, *xy* and *yz* projections; (i) and (j) 2525.64, *xy* and *yz* projections. The electric field direction is along the *x* axis.

GENERAL CONCLUSIONS

At the beginning of our project, we set out to work towards the following objectives:

1. Preparation of electrospun piezoelectric PVDF nanofibers.
2. Preparation of PVDF fiber mat assemblies on electrodes and test their electric properties.
3. Study of inverse piezoelectric actuation of nanofiber mat assemblies.
4. Test the biocompatibility of the PVDF nanofibers.
5. Study the effect of piezoelectric actuation on living cells.

At the end we can say that we achieved the first three objectives completely and the fourth one only partially. We successfully prepared PVDF nanofiber mats with adequate properties for piezoelectric actuation. We also prepared and tested several devices.

The results revealed that electrospinning parameters had significant effects on morphology and crystal phase ratios of PVDF electrospun fibers. As it was expected, the electrical impedance of PVDF decreased with the increase of β crystal phase ratio, which was helpful for the piezoelectric behaviour of the PVDF fibers. The results also illustrated that the impedance of PVDF electroactuator changed with geometric shape. *In vitro* cytocompatibility tests of PVDF scaffolds shown that the NIH3T3 cells cultured on scaffolds were alive which meant PVDF biocompatibility was acceptable for biomedical applications.

However, we didn't observe the vibration of PVDF fibers at low frequency because of lacking some typical instrument, like a laser Doppler vibrometer, though we found some features at the low frequency part of the impedance spectrum, which may be an indication of incipient piezoelectric behavior. Because we could not confirm the vibration in the frequency range needed for cell stimulation, between 0.1 and 10 Hz, we didn't proceed to the last objective of our project: direct cell stimulation with PVDF electroactuator.

From the results we got from this project, we have reasons to believe that it is possible to achieve our initial objectives in future works, we just need more time. Our project has made a promising work for potential applications of PVDF electroactuators in some fields, such as, tissue engineering, electrical devices, smart skin and so on.

REFERENCES

1. Chieh, C.; Fuh, Y.; Lin, L. A direct-write piezoelectric PVDF nanogenerator. 15th *International Conference on Solid-State Sensors, Actuators and Microsystems*. Denver, **2009**, 1485-1488. Doi:10.1109/SENSOR.2009.5285796.
2. Sajkiewicz, P.; Wasiak, A.; Gocłowski, Z. Phase transitions during stretching of poly (vinylidene fluoride). *Eur. Polym. J.* **1999**, 35(3): 423-429.
3. Oshiki, M.; Fukada, E. Inverse piezoelectric effect and electrostrictive effect in polarized poly (vinylidene fluoride) films. *J. Mater. Sci.* **1975**, 10(1): 1-6.
4. Krucińska, I.; Cybula, M.; Rambausek, L.; Langenhove, L. Piezoelectric textiles: state of the art. *Adv. Perform. Mater*. **2010**, 25(2): 93-100.
5. Shao, H.; Fang, J.; Wang, H.; Lin, T. Effect of electrospinning parameters and polymer concentrations on mechanical-to-electrical energy conversion of randomly-oriented electrospun poly (vinylidene fluoride) nanofiber mats. *RSC Adv*. **2015**, 5(19):14345-50.
6. Ahmed, F. E.; Lalia, B. S.; Hashaikeh, R. A review on electrospinning for membrane fabrication: challenges and applications. *Desalination*. **2015**, 356: 15-30.
7. Gopal, R. ;Kaur, S. ;Ma, Z.; Chan, C.; Ramakrishna, S.; Matsuura, T. Electrospun nanofibrous filtration membrane. *J. Membr. Sci.* **2006**, 281(I):581-586.
8. Dong, Z. ; Ma, X. ; Xu, Z. ; You, W.; Li, F. Super hydrophobic PVDF-PTFE electrospun nanofibrous membranes for desalination by vacuum membrane distillation. *Desalination*. **2014**， 347:175-183.
9. Wu, D.; Tang, D.; Cao, J.; Wang, H. Polyvinylidene fluoride and vinylidene fluoride-hexafluoropropylene copolymer blended nanofibre electrolyte membrane and preparation. Chinese Patent, CN101805454A, 2009**.**
10. Pignatello, R. *Advances in Biomaterials Science and Biomedical Applications*, Biofabrication of Tissue Scaffolds in chapter 12; InTech, 2013； ISBN 978-953-51-1051-4, under CC BY 3.0 license.
11. Reznik, S.; Yarin, A.; Theron, A.; Zussman, E. Transient and steady shapes of droplets attached to a surface in a strong electric field. *J. Fluid Mech*. **2004**. 516: 349–377.

12. Wang, X.; Niu, H.; Wang, X.; Lin, T. Large-scale electrospinning of polymer nanofibers using needleless nozzle. *The 38th Textile Research Symposium*, Susono City, Japan, **2009** pp. 117-122.

13. Yuan, X.; Zhao, Y.; Na, H. Method for preparing PVDF super-fine fiber film with good mechanics-performance. Chinese Patent, CN100450598C, 2007.

14. Pan, C.; Yen, C.; Wang, S.; Lai, Y.; Lin, L.; Huang, J.; Kuo, S. Near-field electrospinning enhances the energy harvesting of hollow PVDF piezoelectric fibers. *RSC Adv.* **2015**, 5(103): 85073-85081.

15. Xia, F.; Cheng, Z.; Xu, H.; Li, H.; Zhang, Q.; Kavarnos, G.; Ting, R.; Abdul-Sadek, G.; Belfield, K. High electromechanical responses in a poly (vinylidene fluoride–trifluoroethylene–chlorofluoroethylene) terpolymer. *Adv. Mater.* **2002**, 14(21): 1574-1577.

16. Wang, Z.; Fan, H.; Su, K.; Wen, Z.; Structure and piezoelectric properties of poly (vinylidene fluoride) studied by density functional theory. *Polym*, **2006**, 47(23): 7988-7996.

17. Lu, Y.; Li, Y.; Zhang, S.; Xu, G.; Fu, K.; Lee, H.; Zhang, X. Parameter study and characterization for polyacrylonitrile nanofibers fabricated via centrifugal spinning process. *Eur. Polym. J.* **2013**, 49(12): 3834-3845.

18. Abolhasani, M.; Azimi, S.; Fashandi, H. Enhanced ferroelectric properties of electrospun poly (vinylidene fluoride) nanofibers by adjusting processing parameters. *RSC Adv*. **2015**, 5(75):61277-83.

19. Lanceros-Mendez, S.; Mano, J.; Costa, A.; Schmidt, V. FTIR and DSC studies of mechanically deformed β-PVDF films. *J. Macromol. Sci., Part B: Phys.* **2001**, 40(3-4): 517-527.

20. Chocat, N.; Lestoquoy, G.; Wang, Z.; Rodgers, D.; Joannopoulos, J.; Fink, Y. Piezoelectric fibers for conformal acoustics. *Adv. Mater.* **2012**, 24(39): 5327-5332.

21. Pu, J.; Yan, X.; Jiang, Y.; Chang, C.; Lin, L. Piezoelectric actuation of direct-write electrospun fibers. *Sens. Actuators, A*. **2010**, 164(1): 131-136.

22. Abouraddy, A.; Bayindir, M.; Benoit, G.; Hart, S.; Kuriki, K.; Orf, N.; Shapira, O.; Sorin, F.; Temelkuran, B.; Fink, Y.; Towards multimaterial multifunctional fibres that see, hear, sense and communicate. *Nat. Mater.* **2007**, 6(5): 336-47.

23. Bayindir, M.; Sorin, F.; Abouraddy, A.; Viens, J.; Hart, S.; Joannopoulos, J.; Fink, Y. Metal–insulator–semiconductor optoelectronic fibres. *Nat*, **2004**, 431(7010): 826-829.

24. Darestani, M.; Chilcott, T.; Coster, H. Electrical impedance spectroscopy study of piezoelectric PVDF membranes. *J. Solid State Electrochem.* **2014**, 18(3): 595-605.

25. Guo, H.; Li, Z.; Dong, S.; Chen, W.; Deng, L.; Wang, Y. Piezoelectric PU/PVDF electrospun scaffolds for wound healing applications. *Colloids Surf., B*, **2012**, 96: 29-36.

26. Wittig, R.; Rosenholm, J.; von Haartman, E.; Hemming, J.; Genze, F.; Bergman, L.; Simmet, T.; Lindén, M.; Sahlgren, C. Active targeting of mesoporous silica drug carriers enhances γ-secretase inhibitor efficacy in an in vivo model for breast cancer. *Nanomedicine*, **2014**, 9: 971–987.

27. Rosenholm, J. M.; Sahlgren, C.; Lindén, M. Towards multifunctional, targeted drug delivery systems using mesoporous silica nanoparticles-opportunities & challenges. *Nanoscale*, **2010**, 2: 1870–1883.

28. Miller, L.; Winter, G.; Baur, B. Synthesis, characterization, and biodistribution of multiple 89 Zr-labeled pore-expanded mesoporous silica nanoparticles for PET. *Nanoscale*, **2014**, 6: 4928–4935.

29. Auger, F.; Gibot, L.; Lacroix, D. The pivotal role of vascularization in tissue engineering. *Annu. Rev. Biomed. Eng*, **2013**, 15: 177–200.

30. Rosenholm, J. M.; Sahlgren, C.; Lindén, M. Multifunctional mesoporous silica nanoparticles for combined therapeutic, diagnostic and targeted action in cancer treatment. *Curr. Drug Targets*, **2011**, 12: 1166–1186.

31. Qazi, T.; Rai, R.; Dippold, D.; Roether, J.; Schubert, D.; Rosellini, E.; Barbani, N.; Boccaccini, A. Development and characterization of novel electrically conductive PANI–PGS composites for cardiac tissue engineering applications. *Acta Biomater. 2014*, 10(6): 2434-2445.

32. He, F.; Luo, B.; Yuan, S. PVDF film tethered with RGD-click-poly (glycidyl methacrylate) brushes by combination of direct surface-initiated ATRP and click chemistry for improved cytocompatibility. *RSC Adv*. **2014**, 4:105-17.

33. Xu, T.; Su, J.; Zhang, Q. Electroactive-polymer-based MEMS for aerospace and medical applications. *Proc. SPIE 5055, Smart Structures and Materials 2003: Smart Electronics, MEMS, BioMEMS, and Nanotechnology* , San Diego, CA , **2003**, 24: 66-77.

34. Yu, D.; Zhou, J.; Chatterton, N.; Li, Y. Polyacrylonitrile nanofibers coated with silver nanoparticles using a modified coaxial electrospinning process. *Int. J. Nanomed.* **2012**, 7: 5725.

35. Laroche, G.; Marois, Y.; Schwarz, E. Polyvinylidene Fluoride Monofilament Sutures: Can They Be Used Safely for Long-Term Anastomoses in the Thoracic Aorta?. *Artif. Organs*. **1995**, 19(11):1190-9.

36. Mackay, T.; Bernacca, G. M. In vitro function and durability assessment of a novel polyurethane heart valve prosthesis. *Artif. Organs*, **1996**, 20: 1017–1025.

37. Pizzoferrato, A.; Arciola, C. R.; Cenni, E. In vitro biocompatibility of a polyurethane catheter after deposition of fluorinated film. *Biomaterials*, **1995**, 16: 361–367.

38. Hester, T. R.; Cukic, J. Use of stacked polyurethane-covered mammary implants in aesthetic and reconstructive breast surgery. *Plast. Reconstr. Surg*, **1991**, 88: 503–509.

39. Liu, S. J.; Kau, Y. C.; Chou, C. Y. Electrospun PLGA/collagen nanofibrous membrane as early-stage wound dressing. *J. Membr. Sci*, **2010**, 355: 53–59.

40. Ong, S. Y.; Wu, J.; Moochhala, S. M. Development of a chitosanbased wound dressing with improved hemostatic and antimicrobial properties. *Biomaterials*, **2008**, 32: 4323–4332.

41. Aoyagi, S.; Onishi, H.; Machida, Y. Novel chitosan wound dressing loaded with minocycline for the treatment of severe burn wounds. *Int. J. Pharm*, **2007**, 330: 138–145.

42. Ulubayram, K.; Cakar, A. N.; Korkusuz, P. EGF containing gelatin-based wound dressings. *Biomaterials*, **2001**, 22: 1345–1356.

43. Li, Z.; Qu, Y.; Zhang, X. Bioactive nano-titania ceramics with biomechanical compatibility prepared by doping with piezoelectric BaTiO3. *Acta Biomater*, **2009**, 5: 2189–2195.

44. Bouaziz, A.; Richert, A.; Caprani, A. Vascular endothelial cell responses to different electrically charged poly (vinylidene fluoride) supports under static and oscillating flow conditions. *Biomaterials*, **1997**, 18(2): 107-112.

45. Feng, J.; Yuan, H.; Zhang, X. Promotion of osteogenesis by a piezoelectric biological ceramic. *Biomaterials*, **1997**, 18: 1531–1534.

46. Valentini, R. F.; Vargo, T. G; Gardella, J. A; Aebischer, P. Electrically charged polymeric substrates enhance nerve fiber outgrowth in vitro. *Biomaterials*, **1992**, 13: 183–190.

47. Fine, E. G.; Valentini, R. F.; Bellamkonda, R.; Aebischer, P. Improved nerve regeneration through piezoelectric vinylidenefluoride-trifluoroethylene

copolymer guidance channels. *Biomaterials*, **1991**, 12: 775–780.

48. Guo, H. F.; Ying, X.; Zhang, J. P. A method of preparing functional wound dressing capable of accelerating wound healing. *Chinese Patent, CN102861355 A*. **2012**

49. Yoshimoto, H.; Shin, Y. M.; Terai, H.; Vacanti, J. P. A biodegradable nanofiber scaffold by electrospinning and its potential for bone tissue engineering. *Biomaterials*, **2003**, 24(12): 2077-2082.

50. Zhang, J.; Qiu, K.; Sun, B.; Fang, J.; Zhang, K.; Mo, X. The aligned core–sheath nanofibers with electrical conductivity for neural tissue engineering. *J. Mater. Chem. B*. **2014**, 2:7945-7954

51. Zhao, G.; Zhang, X.; Lu, T.; Xu, F. Recent Advances in Electrospun Nanofibrous Scaffolds for Cardiac Tissue Engineering. *Adv. Funct. Mater.* **2015**, 25(36): 5726-5738.

52. Andrew, J. S.; Clarke, D. R. Effect of electrospinning on the ferroelectric phase content of polyvinylidene difluoride fibers. *Langmuir*, **2008**, 24(6): 670-672.

53. Wang, Y. R.; Zheng, J. M.; Ren, G. Y.; Zhang, P. H.; Xu, C. A flexible piezoelectric force sensor based on PVDF fabrics. *Smart Mater. Struct.* **2011**, 20(5): 45-52.

54. Fang, J.; Niu, H.; Wang, H.; Wang, X.; Lin, T. Enhanced mechanical energy harvesting using needleless electrospun poly(vinylidene fluoride)nanofiber webs. *Energy Environ. Sci*., **2013**, 21(6): 2196-2202.

55. Yee, W. A.; Nguyen, A. C.; Lee, P. S.; Kotaki, M.; Liu, Y.; Tan, B. T; Mhaislakar, S.; Lu, X. Stress-induced structural changes in electrospun polyvinylidene difluoride nanofibers collected using a modified rotating disk. *Polymer*, **2008**, 49 (2): 4196–4203.

56. Yu, H.; Huang, T.; Lu, M.; Mao, M.; Zhang, Q.; Wang, H. Enhanced power output of an electrospun PVDF/MWCNTs-based nanogenerator by tuning its conductivity. *Nanotechnology* , **2013**, 24(10): 401-405.

57. Gheibi, A.; Bagherzadeh, R.; Merati, A. A.; Latifi, M. Electrical power generation from piezoelectric electrospun nanofibers membranes: electrospinning parameters optimization and effect of membranes thickness on output electrical voltage. *J Polym Res*. **2014**, 21: 571.

58. Tang, S. L. P. Recent developments in flexible wearable electronics for monitoring applications. *Trans. Inst. Meas. Control,* **2007**, 29(3-4): 283-300.

59. Swallow, L. M.; Luo, J. K.; Siores, E.; Patel, I.; Dodds, D.A piezoelectric fiber composite based energy harvesting device for potential wearable applications. *Smart Mater. Struct.* **2008**, 17(2): 17-25.

60. Eisenmenger, W.; Schmidt, H.; Dehlen, B. Space charge and dipoles in poly (vinylidenefluoride). *Braz. J. Phys.*, **1999**, 29(6): 295–305.

61. Abdelsayed, I. M. Characterization of electrosprayed poly (vinylidene fluoride) and poly (vinylidene fluoride)/CNTnanocomposite. Master Dissertation. *Science in Engineering: Virginia Commonwealth University*, **2006**.

62. King, T.; Pozzi, M. Structure and piezoelectric properties of poly (vinylidene fluoride) studied by density functional theory. *Polymer*, **2006**, 47(8): 88-96.

63. Gasteiger, J.; Marsili, M. Iterative partial equalization of orbital electronegativity—a rapid access to atomic charges. *Tetrahedron*, **1980**, 36(22): 3219-3228.

64. Tomás, E.; Gómez A. A. Air-coupled piezoelectric transducers with active polypropylene foam matching layers. *Sensors*, **2013**, 13(5): 5996-6013.

65. Wang, S.; Chung, D. D. L. Apparent negative electrical resistance in carbon fiber composites. *Composites, Part B*, **1999**, 30(6): 579-590.

UNIVERSIDADE da MADEIRA

CQM
CENTRO DE QUÍMICA DA MADEIRA

FCT Fundação para a Ciência e a Tecnologia
MINISTÉRIO DA EDUCAÇÃO E CIÊNCIA

Molecular Materials®
RESEARCH GROUP
MADEIRA ISLAND - PORTUGAL

PTNMR

VIDAMAR
RESORTS
MADEIRA

União Europeia

Governo da República Portuguesa

Região Autónoma da Madeira